Available online at www.sciencedirect.com
ScienceDirect
Comput. Methods Appl. Mech. Engrg. 323 (2017) 202–229
Computer methods in applied mechanics and engineering
www.elsevier.com/locate/cma

Coupled ductile–hydrolytic damage model based on variational constitutive updates

Paulo Bastos de Castro[a], Eduardo Alberto Fancello[a,b,*]

[a] GRANTE - Department of Mechanical Engineering, Universidade Federal de Santa Catarina, Florianópolis, SC, Brazil
[b] LEBm - University Hospital, Universidade Federal de Santa Catarina, Florianópolis, SC, Brazil

Received 8 December 2016; received in revised form 2 May 2017; accepted 15 May 2017
Available online 25 May 2017

Abstract

This work presents a constitutive model suitable for the description of materials showing elastic–viscoplastic behavior and coupled ductile–hydrolytic damage. Such behavior is frequently observed in bioabsorbable materials that have been increasingly used in the development of medical implants (surgical sutures, screws, plates, anchors, stents, etc.). An approach for describing this coupling between mechanical and hydrolytic damage is the core and main contribution of the current proposal. The model is embedded within a variational framework in such a way that the update of internal variables is driven by a minimization principle. A complete description of the model is presented as well as operational details related to an incremental algorithm suitable for finite element calculations. Despite the complexity of the phenomena involved in the formulation, it is shown that the update algorithm follows a simple operational scheme. Several numerical tests were carried out at a material point level, showing the model capability to handle coupling effects of ductile and chemical (hydrolytic) damage. Furthermore, some implications related to the dependence of dissipation functions on state variables, mainly those dependent on the elastic state, were analyzed demonstrating the possible consequences on the solution of damage and stress. The material model was successfully implemented in an in-house code and a commercial code, where examples of application on 3D devices were run bringing insight into realistic applications of the proposed model.

Keywords: Variational constitutive updates; Viscoplasticity; Ductile–hydrolytic damage; Finite elements

1. Introduction

Engineering materials, to one degree or another, are susceptible to physical and/or chemical degradation. In general, such processes should be prevented or at least predicted in order to determine the lifespan of components and products. Controlled degradation, however, may be desirable when dealing with environmentally-friendly biodegradable materials, or bioabsorbable medical applications.

* Corresponding author.
E-mail address: eduardo.fancello@ufsc.br (E.A. Fancello).

http://dx.doi.org/10.1016/j.cma.2017.05.023

Over the past decade, an increasing usage of bioabsorbable medical implants, such as screws, suture anchors, stents, has taken place, thus resulting in considerable advances in trauma, orthopedic and vascular procedures. The development of such products demands a sound knowledge about material behavior, experimental tests and numerical simulations. As a consequence, a vast number of theories and models dealing with degradation phenomena has been published.

In the proposal presented by Rajagopal et al. [1], a general framework for modeling strain-induced degradation is set down, wherein physically and/or chemically driven damage models can be promptly accommodated into the formulation. Soares et al. [2,3] extended that previous work by tailoring a particular formulation that accounts for hydrolytic damage effects. Similar approaches appear in [4–7], where alternative damage function and free-energy potentials have been used. Degradation of fiber-reinforced materials has been also investigated in [8] by following those concepts stated in [1]. Furthermore, the modeling of concentration and diffusion [9–11] has contributed to widen the range of applications of damage formulations. In turn, Fancello et al. [12] present a constitutive formulation that associates the hydrolytic degradation phenomenon with the classic Lemaitre's ductile damage model [13,14]. Additional references on hydrolytic degradation models can be found in recent works of Bergstrom and Hayman [15], Bobel et al. [16], Boland et al. [17] Soares and Moore [18]. Finally, it is worth mentioning that models for degrading materials are clearly not limited to polymers. An important example of this is the modeling and simulation of metal corrosion. Papers like [19–23] bring complementary perspective on degradation modeling showing that different chemical degradation phenomena such as hydrolysis and corrosion may fall into similar phenomenological formulations.

Several of these referenced works describe chemical degradation by means of a *degradation field*, say d^h, controlling loss of mechanical properties. Evolution of this field is usually characterized by continuum-based mathematical models conceptually similar to those found in classical continuum damage mechanics. Consequently, despite mechanical damage and chemical degradation may differ at the micromechanical scale, it can be argued that both lead to similar outcome at a macromechanical scale.

A review of the specific literature shows that the interplay between ductile damage and hydrolytic degradation has been neglected, though such correlation is believed to be an important aspect in the mechanical representation of the materials under discussion. It is known that in the presence of finite strains, mechanically induced damage may become increasingly relevant. Moreover, most of the chemical-degradation evolution models are dependent on the current degradation state. Experimental observations show that chemical degradation intensifies mechanical damage and localizations [2,24–26].

An approach for describing these couplings is the core of this current work, wherein its main contribution consists in the extension of an elastic–viscoplastic model to account for coupled ductile–hydrolytic damage within a finite kinematics context. Hydrolytic degradation is incorporated into the model by proposing a dissipation potential whose expression was inspired by chemical-kinetics equations [27,28]. In contrast with other models found in the literature, this potential couples mechanical damage and chemical degradation with significant consequences on the phenomenon description as well as on the numerical treatment of the model.

The model is embedded within the so-called variational constitutive framework by which incremental stress-deformation relations can be consistently derived from pseudo-elastic strain–energy potentials [29,30]. This formalism has been already used in a wide range of applications: living tissues [31–33], multiscale models [34], homogenization of composite materials [35,36], thermo-mechanical coupled problems [37–41], rate-dependent mechanics [42–46], damage mechanics [47–51], error estimation and mesh refining procedures [52,53].

Having as the main goal of this study an evaluation of ductile and chemical degradation couplings, a local damage formulation was initially proposed. As a consequence of this choice, well-known numerical pathologies associated with mesh dependency are expected to appear [54–56]. While several approaches circumvent these difficulties by modifying the local nature of the damage formulation (see [14,56,57]), other recent strategies introduce phase fields and level set concepts in order to regularize local damage models [58–60]. The use of these regularization strategies, however, is beyond the scope of this manuscript.

To offer a comprehensive description of the model, the manuscript is organized as follows. Section 2 is used to briefly present the principles of the variational constitutive updates. The theoretical core of the proposed model is then shown in Section 3. Numerical examples are shown in Section 4. In that section, the main characteristic responses of the model, i.e., coupling effects, material and integration parameters, applicability to finite element simulations and mesh sensitivity are evaluated. Finally, Section 5 closes the manuscript with comments and concluding remarks.

2. Variational constitutive updates

Looking to the definition of basic notation, this section outlines the framework proposed in [29], [30].

Having defined a set of state variables $\mathcal{E} = \{\mathbf{F}, \mathbf{Z}\}$, where $\mathbf{F}$ is the deformation gradient, $\mathbf{Z}$ is a general representation of internal variables, and assuming the existence of a Helmholtz free-energy $W = W(\mathcal{E})$, the constitutive problem can be established by stating the pseudo-potentials

$$\mathcal{P}(\dot{\mathbf{F}}, \dot{\mathbf{Z}}; \mathcal{E}) = \dot{W}(\dot{\mathbf{F}}, \dot{\mathbf{Z}}; \mathcal{E}) + \phi^*(\dot{\mathbf{Z}}; \mathcal{E}) \,, \tag{1}$$

$$\bar{\mathcal{P}}(\dot{\mathbf{F}}; \mathcal{E}) = \inf_{\dot{\mathbf{z}}} \mathcal{P}(\dot{\mathbf{F}}, \dot{\mathbf{Z}}; \mathcal{E}) \,, \tag{2}$$

where $*$ is an appropriate product operation and $\phi^*(\dot{\mathbf{Z}}; \mathcal{E})$ is a convex, non-negative, zero value at the origin, dissipation function. The optimality condition in (2) yields the evolution equation ((3)-a), while the partial derivative of $\bar{\mathcal{P}}$ with respect to $\dot{\mathbf{F}}$ results in the state equation for the first Piola–Kirchhoff stress $\mathbf{P}$ ((3)-b)

$$\frac{\partial W(\mathbf{Z})}{\partial \mathbf{Z}} + \frac{\partial \phi^*(\dot{\mathbf{Z}}; \mathcal{E})}{\partial \dot{\mathbf{Z}}} = 0 \,, \quad \mathbf{P} = \frac{\partial W}{\partial \mathbf{F}} = \frac{\partial \bar{\mathcal{P}}(\dot{\mathbf{F}}; \mathcal{E})}{\partial \dot{\mathbf{F}}}. \tag{3}$$

Similarly, constitutive incremental updates can be obtained by extremization operations on the so-called *incremental potential* defined as:

$$\mathcal{W}(\mathbf{F}_{n+1}, \mathbf{Z}_{n+1}; \mathcal{E}_n) = W(\mathbf{F}_{n+1}, \mathbf{Z}_{n+1}) - W(\mathbf{F}_n, \mathbf{Z}_n) + \Delta t \phi^*(\mathbf{Z}_{n+1}; \mathcal{E}_n) \,, \tag{4}$$

$$\bar{\mathcal{W}}(\mathbf{F}_{n+1}; \mathcal{E}_n) = \inf_{\mathbf{Z}_{n+1}} \mathcal{W}(\mathbf{F}_{n+1}, \mathbf{Z}_{n+1}; \mathcal{E}_n) \,. \tag{5}$$

Again, the minimization in (5) results in an incremental counterpart of the evolution equation, while its partial derivative with respect to $\mathbf{F}_{n+1}$ results in a discrete expression of the stress update:

$$\frac{\partial W_{n+1}}{\partial \mathbf{Z}_{n+1}} + \Delta t \frac{\partial \phi^*(\mathbf{Z}_{n+1}; \mathcal{E}_n)}{\partial \mathbf{Z}_{n+1}} = 0, \tag{6}$$

$$\mathbf{P}_{n+1} = \frac{\partial \bar{\mathcal{W}}}{\partial \mathbf{F}_{n+1}} \quad \text{or} \quad \mathbf{S}_{n+1} = 2 \frac{\partial \bar{\mathcal{W}}}{\partial \mathbf{C}_{n+1}} \,, \tag{7}$$

where $\mathbf{C}_{n+1}$ is the right Cauchy–Green deformation tensor, and $\mathbf{S}_{n+1}$ is the second Piola–Kirchhoff stress.

Considering the satisfaction of compatibility and constitutive equations, the problem of equilibrium may be stated as the minimization of an incremental total-potential energy defined over the undeformed configuration Ω_0 with the boundary Γ_0:

$$\mathbf{x}^*_{n+1} = \arg \min_{\mathbf{x}_{n+1} \in \mathcal{K}} \mathcal{H}(\mathbf{x}_{n+1}) \,, \tag{8}$$

$$\mathcal{H}(\mathbf{x}_{n+1}) = \int_{\Omega_0} \bar{\mathcal{W}}(\mathbf{F}(\mathbf{x}_{n+1})) d\Omega_0 - \left[\int_{\Omega_0} \mathbf{b}_0 \cdot \mathbf{x}_{n+1} \, d\Omega_0 + \int_{\Gamma_0} \mathbf{f}_0 \cdot \mathbf{x}_{n+1} \, d\Gamma_0 \right] , \tag{9}$$

where $\mathbf{b}_0$ and $\mathbf{f}_0$ are the body and surface forces on the reference configuration and $\mathcal{K}$ is the set of admissible deformations. Necessary optimality conditions lead to the well-known Principle of Virtual Work

$$\int_{\Omega_0} \mathbf{P}_{n+1} : \nabla \delta \mathbf{x} \, d\Omega_0 - \left[\int_{\Omega_0} \mathbf{b}_0 \cdot \delta \mathbf{x} \, d\Omega_0 + \int_{\Gamma_0} \mathbf{f}_0 \cdot \delta \mathbf{x} \, d\Gamma_0 \right] = 0, \qquad \forall \delta \mathbf{x} \in \mathcal{V}, \tag{10}$$

being $\mathcal{V}$ the set of virtual deformations.

3. Elastic–viscoplastic model with ductile–hydrolytic damage

3.1. Initial considerations

The viscoplastic model used herein follows the same ideas of Ortiz and Stainier [29], Fancello et al. [43], Brassart and Stainier [46], being the form of the dissipation function one of Perzyna-type. Ductile damaging is formulated in such a fashion it resembles the classic Lemaitre's model and follows the parametrization proposed in [48,49]. The

novelty introduced in this work is the coupled hydrolytic damage potential whose expression is inspired by chemical-kinetics functions such those based on Arrhenius-like equations [27,28]. Despite this contribution is centered in the mechanical–chemical coupling, all terms of the model are described for the sake of clarity and uniform notation.

Within a finite deformation framework, the classical Kröner–Lee multiplicative decomposition $\mathbf{F} = \mathbf{F}^e\mathbf{F}^p$ is used. The plastic tensor $\mathbf{F}^p$ is considered to be isochoric and the velocity gradient $\mathbf{L} = \dot{\mathbf{F}}\mathbf{F}^{-1}$ is split into elastic and plastic contributions:

$$\mathbf{L} = \mathbf{L}^e + \mathbf{F}^e\mathbf{L}^p(\mathbf{F}^e)^{-1}, \quad \mathbf{L}^e \equiv \dot{\mathbf{F}}^e(\mathbf{F}^e)^{-1}, \quad \mathbf{L}^p \equiv \dot{\mathbf{F}}^p(\mathbf{F}^p)^{-1}. \tag{11}$$

The elastic tensor $\mathbf{F}^e$ is again decomposed into isochoric $\hat{\mathbf{F}}^e$ and volumetric $\mathbf{F}^v$ parts, leading to the elastic isochoric form of the right Cauchy–Green deformation tensor $\hat{\mathbf{C}}^e$:

$$\mathbf{F}^e = \hat{\mathbf{F}}^e\mathbf{F}^v\,, \qquad \hat{\mathbf{F}}^e = J^{-\frac{1}{3}}\mathbf{F}^e\,, \qquad \mathbf{F}^v = J^{\frac{1}{3}}\mathbf{I}\,, \qquad \hat{\mathbf{C}}^e = \hat{\mathbf{F}}^{e\,T}\hat{\mathbf{F}}^e, \tag{12}$$

being $J = \det\mathbf{F}$ and $\mathbf{I}$ the second-order identity tensor.

The model is assumed to be dependent on the following set of state variables:

$$\mathcal{E} = \left\{\mathbf{F}, \mathbf{F}^p, \alpha, d^h, d^p\right\}, \tag{13}$$

where α is a scalar internal variable related to a measure of the accumulated plastic strain and d^p is the classical ductile damage. The variable d^h is then introduced as a measure of loss of material properties due to chemical (hydrolysis) degradation in an analogous way as it is done with ductile damage. It is hereafter assumed that both d^p and d^h can be treated as damage-like variables that contribute additively to the total damage d:

$$d = d^p + d^h. \tag{14}$$

The free-energy potential W with linear dependence on d is additively decomposed into isochoric elastic W^e, plastic W^p and volumetric elastic U contributions:

$$W = (1-d)\left[W^e(\hat{\mathbf{C}}^e) + W^p(\alpha) + U(J)\right]. \tag{15}$$

It is worth noting that, as in [48], all elastic and plastic terms are multiplied by the total damage d, which is a stark difference with respect to the classic Lemaitre's model. Thus, the influence of damage on the plastic potential results into a progressive reduction of the material hardening capacity. Following the conventional Coleman–Noll procedure the following conjugate forces are obtained:

$$\mathbf{P} = \frac{\partial W}{\partial \mathbf{F}}, \qquad \chi = \frac{\partial W}{\partial \mathbf{F}^p}, \qquad \kappa = \frac{\partial W}{\partial \alpha}, \tag{16}$$

$$-Y^p = \frac{\partial W}{\partial d^p}, \qquad -Y^h = \frac{\partial W}{\partial d^h}, \tag{17}$$

where, owing to the definition of d, one has

$$Y^p = Y^h = Y = -\frac{\partial W}{\partial d} = W^e(\hat{\mathbf{C}}^e) + W^p(\alpha) + U(J). \tag{18}$$

In other words, the variable Y quantifies the total free energy that would be stored by an undamaged material for a given strain history.

Two constraints are then enforced between the internal variables. The first one relates $\mathbf{F}^p$ and α by means of the non-holonomic parametrization [29]

$$\mathbf{D}^p = \mathbf{L}^p = \dot{\mathbf{F}}^p\left(\mathbf{F}^p\right)^{-1} = \dot{\alpha}\mathbf{M}\,, \tag{19}$$

$$\mathbf{M} \in \mathcal{K}_{\mathrm{M}} = \left\{\mathbf{N} \in \mathtt{Sym.}; \mathbf{N} : \mathbf{N} = \frac{3}{2}; \mathbf{N} : \mathbf{I} = 0\right\}\,, \tag{20}$$

where $\mathbf{D}^p$ is the plastic stretching tensor (rate of plastic deformation), and the usual assumption of a null plastic spin $\mathbf{W}^p = 0$ is employed. The scalar variable $\dot{\alpha} \geq 0$ measures the stretching amplitude, while the tensor $\mathbf{M}$ defines the stretching direction.

The second (non-holonomic) constraint associates the plastic damage d^p with α by means of the following evolution law:

$$\dot{d}^p = \dot{\alpha}\frac{Y^S}{N}, \tag{21}$$

where S and N are material constants. Note that this parametrization is nothing but an alternative expression of Lemaitre's law for ductile damage and it was already used in the same variational context by Kintzel et al. [48], Kintzel and Mosler [49]. Both constraints (19) and (21) allow for a considerable reduction of the number of independent state variables.

In accordance with the general framework shown in Section 2, a suitable dissipation function ϕ^* is needed. Within the present proposition, ϕ^* comprises viscoplastic, ductile damage and hydrolytic contributions, respectively:

$$\phi^* = \psi^*_{vp} + \varphi^*_{dp} + \varphi^*_{dh} \,. \tag{22}$$

3.2. Viscoplastic dissipation function

The viscoplastic potential ψ^*_{vp} has the following Perzynas's function structure:

$$\psi^*_{vp} = \begin{cases} (1-d)\,\sigma_Y \dot{\alpha} + \dfrac{\mathtt{c}\, f_A(\alpha)}{\eta+1}\left(\dfrac{\dot{\alpha}}{\mathtt{c}}\right)^{\eta+1} & \text{if } \dot{\alpha} \geq 0 \\ +\infty & \text{if } \dot{\alpha} < 0, \end{cases} \tag{23}$$

where σ_Y is the initial yield stress, $f_A(\alpha)$ is a function associated with material viscoplastic saturation [61], and η and $\mathtt{c}$ are material constants.

3.3. Ductile-damage dissipation function

The ductile-damage dissipation function φ^*_{dp} is given by

$$\varphi^*_{dp} = \begin{cases} \dot{d}^{\,p} Y = \dot{\alpha}\dfrac{Y^{S+1}}{N} & \text{if } \dot{\alpha} \geq 0 \\ +\infty & \text{if } \dot{\alpha} < 0, \end{cases} \tag{24}$$

where the parametrization (21) allows this potential to be written in terms of $\dot{\alpha}$.

3.4. Hydrolytic-damage dissipation function

During hydrolysis, water molecules attack polymer weak bonds producing the scission of long chains. The rate of bond scissions $\dot{b}$ is usually modeled by chemical-kinetics equations of the type $\dot{b} = k_b C\,(b)$, where C represents the number of weak bonds present in long chains per unit volume and k_b is a reaction constant that depends on temperature and activation energy, among other factors. As more scissions occur, the number C decreases, reducing the bonds available for water molecules to attack [27,28]. If we relate bond scissions to a measure of material degradation, a possible form for the latter evolution equation is given by

$$\dot{d}^h = k_d (1-d^h)^n \,, \tag{25}$$

where the exponent n is usually known as the order of reaction. Considering an isothermal process, the reaction constant k_d is assumed to be dependent on mechanical actions. Within these hypotheses, a convenient evolution equation for degradation measure takes the form

$$\dot{d}^h = \frac{(Y+g)^m}{R}(1-d)^n. \tag{26}$$

In this expression the material constant g guarantees the evolution of d^h even in the absence of mechanical actions, which are represented in (26) by the conjugate force Y. The material constants R and m complete the characterization of k_d in (25). Note also on the right hand of (26) that, differently from (25), the degree of material integrity is characterized by the total damage d, coupling $\dot{d}^h$ with the mechanically induced damage.

As frequently happens, the inspiration for specific potential expressions comes from the expected forms of their derivatives (variations). In the present case, Eq. (26) motivated the following hydrolytic-damage dissipation function:

$$\varphi^*_{dh} = \begin{cases} \dfrac{R}{2(1-d)^n (Y+g)^{m-1}}\,\dot{d}^{\,h\,2} - g\,\dot{d}^h & \text{if } \dot{d}^h \geq 0 \\ +\infty & \text{if } \dot{d}^h < 0. \end{cases} \tag{27}$$

As already mentioned, coupling effects are introduced by the presence of the total damage variable ($d = d^p + d^h$) and also implicitly by the thermodynamic force Y. It is later verified that the stationary condition required for the variational principle recovers the appropriate evolution equation.

3.5. Continuum formulation

In order to set down the variational formulation of the present model, let the so-called effective thermodynamic forces be defined as

$$\tilde{\mathbf{P}} = \frac{\mathbf{P}}{(1-d)}, \qquad \tilde{\boldsymbol{\chi}} = \frac{\boldsymbol{\chi}}{(1-d)}, \qquad \tilde{\kappa} = \frac{\kappa}{(1-d)}\,. \tag{28}$$

By using the definitions (15), (23), (24) and (27) , the pseudo-potentials $\mathcal{P}$ and $\bar{\mathcal{P}}$ take the forms

$$\mathcal{P}(\dot{\mathbf{F}},\dot{\alpha},\mathbf{M},\dot{d}^h;\mathcal{E}) = \dot{W}(\dot{\mathbf{F}},\dot{\alpha},\mathbf{M},\dot{d}^h;\mathcal{E}) + \phi^*(\dot{\alpha},\dot{d}^h;\mathcal{E})\,, \tag{29}$$

$$\bar{\mathcal{P}}(\dot{\mathbf{F}};\mathcal{E}) = \inf_{\dot{\alpha}\geq 0,\,\boldsymbol{M}\in\mathcal{K}_{\mathrm{M}},\dot{d}^h\geq 0} \mathcal{P}(\dot{\mathbf{F}},\dot{\alpha},\mathbf{M},\dot{d}^h;\mathcal{E})\,. \tag{30}$$

Since $\mathbf{M} \in \mathcal{K}_{\mathrm{M}}$, the minimization along such a variable in (30) must be performed considering the corresponding constraints. It is shown in Appendix B that a closed expression of the flow direction $\mathbf{M}$ is obtained:

$$\mathbf{M} = \sqrt{\frac{3}{2}}\frac{\tilde{\boldsymbol{\Sigma}}^e_d}{\left\|\tilde{\boldsymbol{\Sigma}}^e_d\right\|}, \qquad \tilde{\boldsymbol{\Sigma}}^e_d = \mathrm{dev}\left(2\mathbf{C}^e\frac{\partial W^e}{\partial \mathbf{C}^e}\right), \tag{31}$$

where $\tilde{\boldsymbol{\Sigma}}^e_d$ is the deviatoric component of the elastic Mandel effective stress tensor. Moreover, the optimality condition for the minimization along $\dot{\alpha} \geq 0$ provides two possible solutions. If

$$\left.\frac{\partial \mathcal{P}}{\partial \dot{\alpha}}\right|_{\dot{\alpha}=0^+} \geq 0, \tag{32}$$

then the minimum of $\mathcal{P}$ is achieved at $\dot{\alpha} = 0$, that is, no inelastic flow occurs. Otherwise, there exists a value $\dot{\alpha} > 0$ that satisfies the stationary condition

$$\frac{\partial \mathcal{P}}{\partial \dot{\alpha}} = (1-d)\left[(\sigma_Y + \tilde{\kappa}) - \tilde{\Sigma}_{eq}\right] + f_A(\alpha)\left(\frac{\dot{\alpha}}{\mathsf{c}}\right)^{\eta} = 0, \tag{33}$$

where $\tilde{\Sigma}_{eq} = \tilde{\boldsymbol{\Sigma}}^e_d : \mathbf{M}$ is a von Mises-like equivalent stress associated with the effective elastic Mandel tensor. The resulting expression (33) is nothing but a classical viscoplastic flow rule, where the last term quantifies the overstress due to viscous flow (flow resistance). For the sake of modeling simplicity, this term was chosen not to be directly affected by damage; however, experimental studies should be run in order to assess this choice. The eventual need of damage dependence could be easily handled by modifying the potential (23).

The corresponding optimality condition for the minimization in $\dot{d}^h$ is given by

$$\frac{\partial \mathcal{P}}{\partial \dot{d}^h} = -Y + \frac{R}{(1-d)^n (Y+g)^{m-1}}\dot{d}^h - g = 0, \tag{34}$$

which, conveniently written, recovers the expected evolution law for the hydrolytic damage:

$$\dot{d}^h = (1-d)^n \frac{(Y+g)^m}{R}. \tag{35}$$

3.6. Incremental formulation

Aiming at setting up an incremental updating rule for the state variables, the following approximations are defined

$$\dot{\alpha} = \frac{\Delta\alpha}{\Delta t}, \qquad \dot{d}^h = \frac{\Delta d^h}{\Delta t}, \qquad \Delta d^p = \Delta\alpha\frac{Y^S}{N}\,, \tag{36}$$

where $\Delta(\cdot) = (\cdot)_{n+1} - (\cdot)_n$. Then, it is possible to define the potentials

$$\mathcal{W} = \left[W(\mathcal{E}_{n+1}) - W(\mathcal{E}_n)\right] + \Delta t \phi^* \left(\mathbf{M}, \Delta\alpha, \Delta d^h\right), \tag{37}$$

$$\bar{\mathcal{W}}(\mathcal{E}_{n+1}; \mathcal{E}_n) = \inf_{\Delta\alpha\geq 0, \mathbf{M}\in\mathcal{K}_{\mathrm{M}}, \Delta d^h \geq 0} \mathcal{W}(\mathcal{E}_{n+1}; \mathcal{E}_n), \tag{38}$$

where W is given by (15) and ϕ^* is taken here as the incremental version of the dissipative potential (22), that after convenient changes in its arguments results in

$$\begin{aligned}\phi^* = (1 - d_{n+1})\,\sigma_Y \frac{\Delta\alpha}{\Delta t} + \frac{\mathsf{c}\, f_A(\alpha_{n+1})}{\eta + 1}\left(\frac{\Delta\alpha/\Delta t}{\mathsf{c}}\right)^{\eta+1} \\ + Y_{n+1}\frac{\Delta d^p}{\Delta t} + \frac{R}{2(1 - d_{n+\theta})^n \left(Y_{n+\gamma} + g\right)^{m-1}}\left(\frac{\Delta d^h}{\Delta t}\right)^2 - g\frac{\Delta d^h}{\Delta t}.\end{aligned} \tag{39}$$

The symbols $d_{n+\theta}$ and $Y_{n+\gamma}$ represent intermediate values of the corresponding state variables within a time step (see Appendix A). Partial implicit/explicit rules are achieved depending on the choice of these parameters. The reader may ask why some of these variables assume an intermediate value while others are chosen to be full implicit $(n+1)$. The answer is simple: just a matter of convenience and efficiency of the corresponding updating rule. The convenience of this approximation is further investigated with the aid of numerical experiments. Moreover, it is easily verified that expression (39) consistently converges to (22) when Δt goes to zero.

The minimization problem (38) is solved at each time increment for a given $\mathbf{F}_{n+1}$, providing the minimizer set $\{\Delta\alpha, \mathbf{M}, \Delta d^h\}$ and consequently the incremental updated state $\mathcal{E}_{n+1}$.

Some intermediate operational choices should be helpful in order to turn the minimization procedure analytically tractable. The first one is to use the well-known exponential mapping [62] to update the state tensor $\mathbf{F}^p_{n+1}$ for a given increment $\Delta\alpha$ and a direction $\mathbf{M}$,

$$\mathbf{F}^p_{n+1} = \exp\left[\Delta t \mathbf{D}^p\right]\mathbf{F}^p_n = \exp\left[\Delta\alpha \mathbf{M}\right]\mathbf{F}^p_n. \tag{40}$$

The others are defined by expressions relating the updated tensor $\mathbf{F}^p_{n+1}$ to the elastic deformation $\hat{\mathbf{C}}^e_{n+1}$ and the usage of a logarithmic strain $\hat{\boldsymbol{\varepsilon}}^e_{n+1}$:

$$\hat{\mathbf{F}}^e_{n+1} = \hat{\mathbf{F}}_{n+1}\mathbf{F}^{p-1}_{n+1}, \tag{41}$$

$$\hat{\mathbf{C}}^e_{n+1} = \hat{\mathbf{F}}^{eT}_{n+1}\hat{\mathbf{F}}^e_{n+1} = \hat{\mathbf{C}}^{pr}_{n+1}\left[\exp\left(\Delta\alpha\mathbf{M}\right)\right]^{-2}, \tag{42}$$

$$\hat{\mathbf{C}}^{pr}_{n+1} = \mathbf{F}^{p-T}_n \hat{\mathbf{C}}_{n+1}\mathbf{F}^{p-1}_n, \tag{43}$$

$$\hat{\boldsymbol{\varepsilon}}^e_{n+1} = \tfrac{1}{2}\ln\hat{\mathbf{C}}^e_{n+1} = \boldsymbol{\varepsilon}^{pr}_{n+1} - \Delta t\mathbf{D}^p, \tag{44}$$

$$\boldsymbol{\varepsilon}^{pr}_{n+1} = \tfrac{1}{2}\ln\hat{\mathbf{C}}^{pr}_{n+1}, \tag{45}$$

where $(\cdot)^{pr}$ indicates predictor quantities. Eq. (42) is valid only if $\hat{\mathbf{C}}^{pr}_{n+1}$ and $\mathbf{D}^p$ are assumed colinear, allowing permutation between both tensors [29]. This hypothesis is later confirmed as a consequence of the extremization procedure. In a completely analogous way to (30), the minimization along the constrained tensor $\mathbf{M}$ is calculated by means of a Lagrangian function. It is shown in Appendix B that, if the elastic potential W^e is a quadratic function of the logarithmic strain, i.e., a Hencky elastic potential ($\mathbb{D}$ is a fourth-order elastic tensor)

$$W^e = \frac{1}{2}\hat{\boldsymbol{\varepsilon}}^e : \mathbb{D} : \hat{\boldsymbol{\varepsilon}}^e,$$

the minimization results in the following explicit form for the tensor $\mathbf{M}$:

$$\mathbf{M} = \sqrt{\frac{3}{2}}\frac{\hat{\mathbf{C}}^{pr}_{n+1}}{\left\|\hat{\mathbf{C}}^{pr}_{n+1}\right\|}. \tag{46}$$

Once $\mathbf{M}$ has been determined, the optimality conditions related to the scalars $\Delta\alpha$ and Δd^h are evaluated in a two-step procedure. Firstly, a (predictor) elastic-like step is tested assuming $\Delta\alpha = 0$ and looking for $\Delta d^h > 0$ which satisfies

$$\left.\frac{\partial\mathcal{W}}{\partial\Delta d^h}\right|_{\Delta\alpha=0^+} = 0. \tag{47}$$

Considering Δd^h, the following condition is verified

$$\left.\frac{\partial \mathcal{W}}{\partial \Delta\alpha}\right|_{\Delta\alpha=0^+} \geq 0\,. \tag{48}$$

In such a case, the minimum of $\mathcal{W}$ is attained at $\Delta\alpha = 0$ and the step is effectively elastic-like, being the pair obtained $(\Delta\alpha, \Delta d^h)$ the correct updating variables. If, conversely, the derivative (48) results in a negative slope, it turns out that $\Delta\alpha > 0$, and a new pair $(\Delta\alpha, \Delta d^h)$ is sought in order to satisfy the stationary conditions

$$r_1 = \frac{\partial \mathcal{W}}{\partial \Delta\alpha} = \mathcal{G}\frac{\partial W^e_{n+1}}{\partial \Delta\alpha} + \mathtt{A} + \Delta t\mathtt{B} = 0, \tag{49}$$

$$\begin{aligned} r_2 = \frac{\partial \mathcal{W}}{\partial \Delta d^h} = &-(Y_{n+1}+g) + \frac{R}{(1-d_{n+\theta})^n\left(Y_{n+\gamma}+g\right)^{m-1}}\frac{\Delta d^h}{\Delta t} \\ &+ \Delta t\left[\theta\frac{nR}{2(1-d_{n+\theta})^{n+1}\left(Y_{n+\gamma}+g\right)^{m-1}}\left(\frac{\Delta d^h}{\Delta t}\right)^2 - \sigma_Y\left(\frac{\Delta\alpha}{\Delta t}\right)\right] = 0, \end{aligned} \tag{50}$$

where $\mathcal{G}$, $\mathtt{A}$ and $\mathtt{B}$ are expressions given by

$$\begin{aligned} \mathcal{G} = &(1-d_{n+1}) + \Delta t\frac{\Delta\alpha}{\Delta t}\frac{Y^S_{n+1}}{N} - \Delta t\,\sigma_Y\left(\frac{\Delta\alpha}{\Delta t}\right)S\Delta\alpha\frac{Y^{S-1}_{n+1}}{N} \\ &+ \Delta t\frac{R}{2}\left(\frac{\Delta d^h}{\Delta t}\right)^2\gamma\frac{1-m}{(1-d_{n+\theta})^n\left(Y_{n+\gamma}+g\right)^m} \\ &+ \Delta t\frac{R}{2}\left(\frac{\Delta d^h}{\Delta t}\right)^2\theta^2\frac{n}{(1-d_{n+\theta})^{n+1}\left(Y_{n+\gamma}+g\right)^{m-1}}S\Delta\alpha\frac{Y^{S-1}_{n+\theta}}{N}\,, \end{aligned} \tag{51}$$

$$\mathtt{A} = \mathcal{G}\kappa + (1-d_{n+1})\,\sigma_Y + f_A(\alpha_{n+1})\left(\frac{\Delta\alpha/\Delta t}{\mathtt{c}}\right)^{\eta}, \tag{52}$$

$$\begin{aligned} \mathtt{B} = &\frac{\mathtt{c}}{\eta+1}\left(\frac{\Delta\alpha/\Delta t}{\mathtt{c}}\right)^{\eta+1}\frac{\partial f_A(\alpha_{n+1})}{\partial\Delta\alpha} - \sigma_Y\frac{\Delta\alpha}{\Delta t}\frac{Y^S_{n+1}}{N} \\ &+ \frac{R}{2}\left(\frac{\Delta d^h}{\Delta t}\right)^2\theta\frac{n}{(1-d_{n+\theta})^{n+1}\left(Y_{n+\gamma}+g\right)^{m-1}}\frac{Y^S_{n+\theta}}{N}\,. \end{aligned} \tag{53}$$

The above two-step procedure is analogous to the elastic-predictor plastic-corrector schemes of traditional return-mapping algorithms.

Finally, as a consequence of parametrization ((36)-c), the remaining incremental variable Δd^p is simply updated by means of

$$\Delta d^p = \Delta\alpha\frac{Y^S_{n+1}}{N}.$$

After computing the updated state of the incremental variables, the second Piola–Kirchhoff stress is expressed as

$$\mathbf{S}_{n+1} = 2\frac{\partial\bar{\mathcal{W}}}{\partial\mathbf{C}_{n+1}} \equiv 2\frac{\partial\mathcal{W}}{\partial\mathbf{C}_{n+1}} = \mathcal{G}\tilde{\mathbf{S}}_{n+1}\,, \tag{54}$$

where the effective stress $\tilde{\mathbf{S}}_{n+1}$ is given by the classical form

$$\tilde{\mathbf{S}}_{n+1} = 2\frac{\partial Y_{n+1}}{\partial\mathbf{C}_{n+1}} = J^{-2/3}_{n+1}\mathbb{P} : \left(2\frac{\partial W^e_{n+1}}{\partial\hat{\mathbf{C}}_{n+1}}\right) + \frac{\partial U_{n+1}}{\partial J_{n+1}}J_{n+1}\mathbf{C}^{-1}_{n+1}\,, \tag{55}$$

$$\mathbb{P} = \mathbb{I}_s - \frac{1}{3}\left(\mathbf{C}^{-1}_{n+1}\otimes\mathbf{C}_{n+1}\right)\,. \tag{56}$$

3.7. Consistent tangent operator

In a numerical framework, the computation of a consistent tangent operator may be necessary, for example, when a Newton–Raphson scheme is employed to find the global equilibrium for the finite element solution. The derivation of such a consistent tangent modulus results in geometric and material related terms, being that the geometric contribution is identical to that provided for a hyperelastic formulation, whereas the terms associated to the material are given by

$$\mathbb{C} = 4\frac{\mathsf{d}}{\mathsf{d}\mathbf{C}_{n+1}}\left(\frac{\mathsf{d}\mathcal{W}}{\mathsf{d}\mathbf{C}_{n+1}}\right) = 2\frac{\mathsf{d}\left(\mathcal{G}\tilde{\mathbf{S}}_{n+1}\right)}{\mathsf{d}\mathbf{C}_{n+1}}\,, \tag{57}$$

or, after applying the product rule,

$$\mathbb{C} = 2\mathcal{G}\frac{\mathsf{d}\tilde{\mathbf{S}}_{n+1}}{\mathsf{d}\mathbf{C}_{n+1}} + 2\tilde{\mathbf{S}}_{n+1}\otimes\frac{\mathsf{d}\,\mathcal{G}}{\mathsf{d}\mathbf{C}_{n+1}}. \tag{58}$$

Having described the general formulation, some numerical examples and results are shown in the next section in order to evaluate the main capabilities of this model.

4. Examples and results

In this section, response features of the proposed model are presented and evaluated by means of numerical examples. Tests are performed considering three different scenarios. First, homogeneous uniaxial conditions, including relaxation and creep tests, are taken into account in order to present some characteristics intrinsically related to the constitutive model (material response and influence of numerical parameters). Second, tests are carried out on a finite element model of a notched cylindrical bar, also considering uniaxial tensile conditions. Experiments on notched bars are common procedure performed in laboratories aiming at characterization and validation of material models. Additionally, a mesh sensitivity analysis was performed in order to discuss some issues related to the local nature of the damage formulation. Finally, an example based on a typical component made of bioabsorbable materials is presented by means of a simple simulation of a suture anchor. The latter brings some insight into more realistic applications of the proposed constitutive formulation.

It is worth highlighting that the proposed material model was successfully implemented in two codes: an in-house code for finite kinematics called *CEOS* and the commercial code ABAQUS throughout UMAT routines. Simulations provided identical results in comparison tests run with the same element formulation in both codes.

Before presenting the examples, some additional information about the model is required. In order to represent the viscoplastic response, particular choices should be made with respect to the hardening and saturation functions. In this study, a classical form is adopted for the free-energy plastic term $W^p(\alpha)$, resulting into a hardening function $\kappa(\alpha)$ of Voce-like form, that is,

$$\kappa = \frac{\partial W^p}{\partial \alpha} = H\left(1 - e^{-n\alpha}\right) + k\alpha, \tag{59}$$

where

$$W^p = H\alpha + \frac{H\left(e^{-n\alpha} - 1\right)}{n} + \frac{1}{2}k\alpha^2, \tag{60}$$

and H, n, k are material constants.

By following [46], the viscoplastic saturation $f_A(\alpha)$ is taken as a linear function of the accumulated plastic strain:

$$f_A(\alpha) = k_v + h\alpha, \tag{61}$$

being k_v and h constants. These specific hardening and saturation functions are not in any way unique and several different forms can be proposed and easily adapted to the current formulation.

A set of 16 constitutive parameters is to be defined in order to represent a specific material. The numerical tests of Sections 4.1–4.3 were run considering a hypothetical material with parameters given in Table 1. These parameters were chosen aiming to provide numerical results that best illustrate the inherent coupling features of the proposed formulation. Care was taken, however, to keep these values within bounds expected for glassy polymeric materials.

Table 1
Constitutive material parameters.

Material parameter	Symbol	Value
Shear modulus (MPa)	μ	492.960
Bulk modulus (MPa)	K	1998.027
Linear isotropic hardening modulus (MPa)	k	17.5
Isotropic hardening modulus (MPa)	H	5.2
Isotropic hardening exponent	n	140
Yield stress (MPa)	σ_Y	120
Viscoplasticity exponent (rate sensitive)	η	0.2
Viscoplasticity constant (viscosity, 1/s)	c	1.1
Saturation function modulus (MPa)	h	0
Saturation function constant (MPa)	k_v	100
Plastic damage exponent	S	2
Plastic damage constant $(J/mm^3)^S$	N	550
Hydrolytic damage exponent	m	1.5
Hydrolytic damage exponent (damage sensitivity)	$\mathtt{n}$	1
Hydrolytic damage constant $(J/mm^3)^{\mathtt{m}}$	R	125×10^6
Hydrolytic damage constant (J/mm^3)	g	0.1

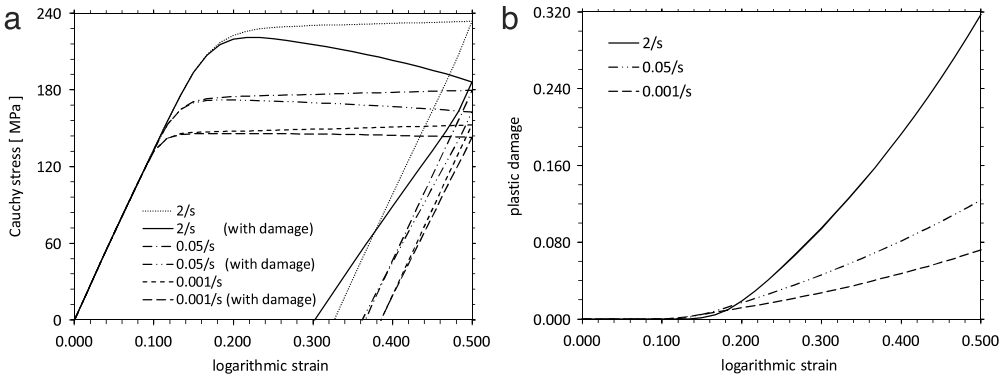

Fig. 1. (a) Influence of strain rate and plastic damage on stress–strain curves. (b) Plastic damage vs. total logarithmic strain at three different strain rates.

The numerical example of Section 4.4, on the other hand, was run considering an identification procedure from experimental data provided in [63].

Finally, it is worth mentioning that hereafter all displayed results of stress refer to nominal (homogenized) Cauchy stress, in contrast with effective stresses defined in (28).

4.1. Relaxation and creep tests under uniaxial stress states

A uniaxial homogeneous loading–unloading stress state controlled by an axial strain history is initially simulated. Three constant strain rates are employed, 0.001, 0.05, 2 s^{-1}, and for all of them, a maximum logarithmic strain of 0.5 is reached.

In Fig. 1(a), viscoplastic and plastic damage effects on Cauchy stress vs. logarithmic strain curves can be observed. The plastic damage is remarkably noticed by the decay of the Cauchy stress during the loading stage, as well as in the decrease of the elastic slope in the unloading procedure. The effects of the strain rate on plastic damage evolution is shown in Fig. 1(b). The higher the strain rate, the higher the final material degradation.

By considering the final state of the loading procedure, and then keeping the total strain constant, a relaxation process involving viscous and degradation effects is observed. Two stages are noticed. In Fig. 2(a), the viscoplastic relaxation that occurs in the first 40 s is presented, where three different initial conditions of stress and plastic damage are observed (due to the short period of time considered, hydrolytic degradation is null). It should be noticed that,

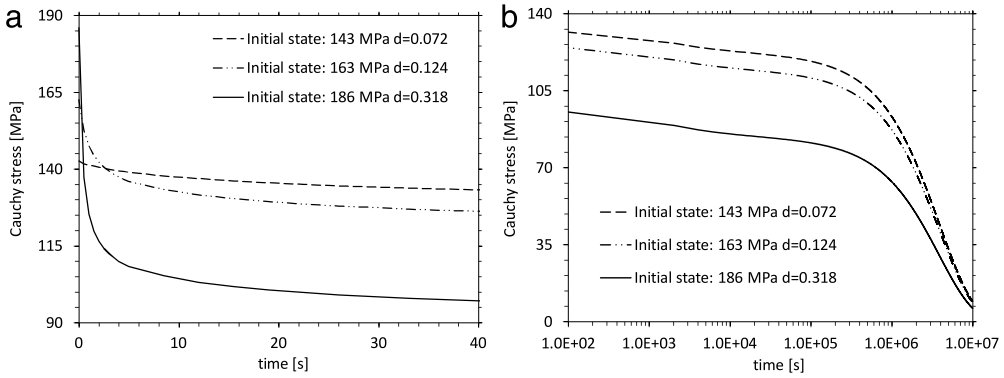

Fig. 2. Relaxation curves for different initial states of stress and plastic damage.

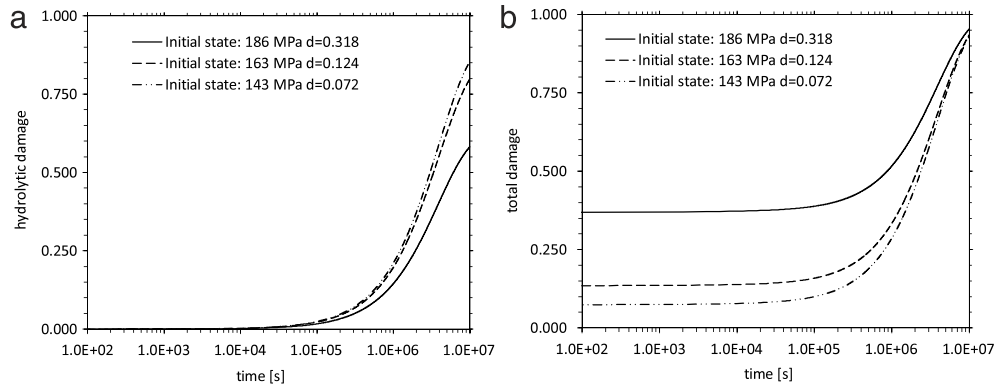

Fig. 3. Evolution of hydrolytic (a) and total damage (b) for different initial states of stress and plastic damage.

for undamaged materials, all relaxation curves would decrease asymptotically to the same stress level. However, as the material is already damaged, the viscoplastic relaxation leads to different final values of stress in each case. Considering the subsequent period of time, from 10^2 s up to 10^7 s (∼115 days), Fig. 2(b) indicates how the hydrolytic degradation acts on the material.

Damage evolution curves are shown in Fig. 3. As degradation progresses, there exists a reduction in damage rates as a consequence of the chosen evolution law (26).

A creep test is also simulated following a procedure similar to that used for relaxation. A total load of 112 N is progressively applied during 28 s on an initial transverse area of 1 mm^2 reaching a (homogenized) Cauchy stress of 120.018 MPa.

The influence of hydrolytic damage on the material behavior is made clear in Fig. 4, in which the evolution of logarithmic strain and Cauchy stress are shown. Two distinct situations are compared, whether hydrolytic degradation is taken into account (continuous line) or not (dashed line).

4.2. Analysis of time integration rules

In this section the influence of the time integration parameters θ and γ are evaluated. These parameters define the intermediate values $d_{n+\theta}$ and $Y_{n+\gamma}$, leading to a full implicit scheme when $\theta = 1$, $\gamma = 1$, or partial midpoint rules for any other assumed combination. Thus, tests are performed such as described below.

First, the same relaxation tests previously presented were carried out by using a time increment of $\Delta t = 2000$ s (a small increment if compared with the time scale $t = 10 \times 10^6$ s of the experiment) in order to establish a reference solution. Then, by setting the parameters (θ, γ) respectively as (1, 1), (0, 0), (1, 0), (0, 1), and proceeding

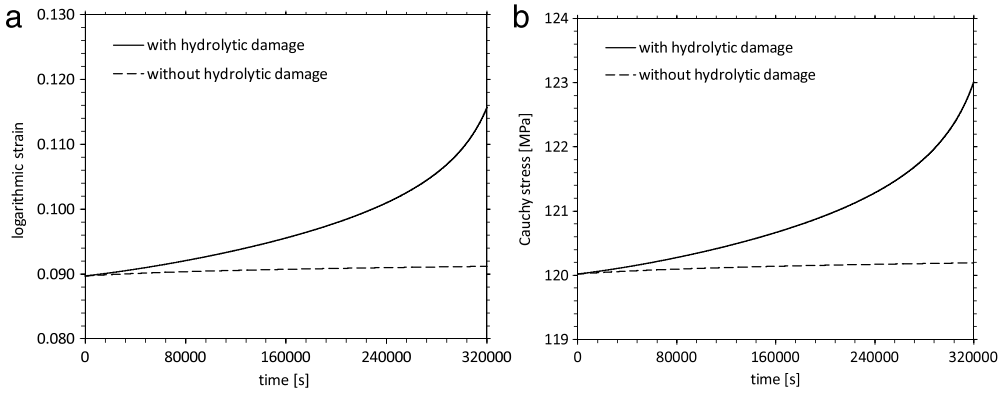

Fig. 4. Influence of damage effects on strain and stress evolution under a constant load of 112 N.

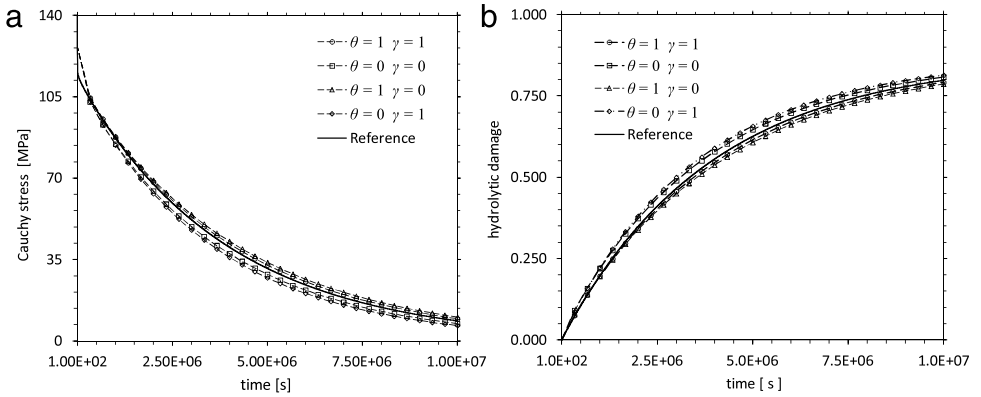

Fig. 5. Evaluation of integration parameters θ, γ, and how they may affect the stress and the hydrolytic damage solutions under relaxation conditions.

with the evaluation for larger time increments ($\Delta t = 333333.3$ s), one has the stress and hydrolytic damage curves shown in Fig. 5. These results were obtained with a strain rate of 0.05 s^{-1}, and the higher errors are found when $\theta = 1, \gamma = 0$, or $\theta = 0, \gamma = 1$. Though not presented here, similar response is produced for the other strain rates (0.001 and 2 s^{-1}).

Another numerical experiment regarding the parameters θ and γ consists in a tensile test for a very low strain rate $\dot{\varepsilon} = 5 \times 10^{-8}$ s^{-1}. In such a test, a total logarithmic strain of 0.5 is reached after $t = 10 \times 10^6$ s (∼115 days). The parameters θ and γ are defined in the same way as before, and time increments are set respectively as $\Delta t = 2000$ s for the reference curve, and $\Delta t = 333333.3$ s for all other cases. As shown in Fig. 6, results diverge from the reference, and the best approach might be considered that for $\theta = 1, \gamma = 0$.

Fig. 7 displays the relative error between the computed stress and the reference value at the corresponding times $t = 5 \times 10^6$ s in the relaxation cases, and $t = 6.7 \times 10^6$ s in the very low rate tests, both being specific times were the greatest errors were observed.

4.3. Tests on a notched cylindrical bar

In this example a non-homogeneous strain problem is tested. A finite element model of a notched cylindrical bar is employed to simulate a tensile test, as well as relaxation and creep conditions. Geometry and dimensions of the model are shown in Fig. 8. Due to the symmetrical configuration of this model, one eighth of the geometry is used in this simulation, where 20-node hexahedral elements with reduced integration were employed.

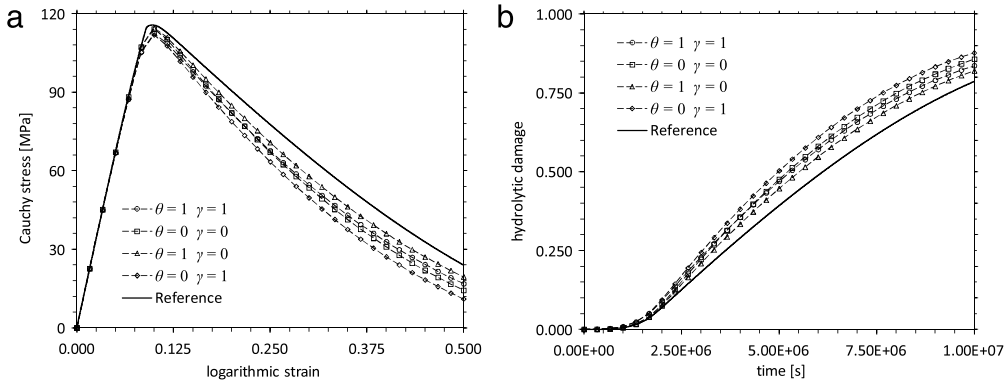

Fig. 6. Evaluation of integration parameters, and how they affect the solution for stress and hydrolytic damage under a uniaxial controlled-displacement test at very low strain rate ($\dot{\epsilon} = 5 \times 10^{-8}$ s^{-1}).

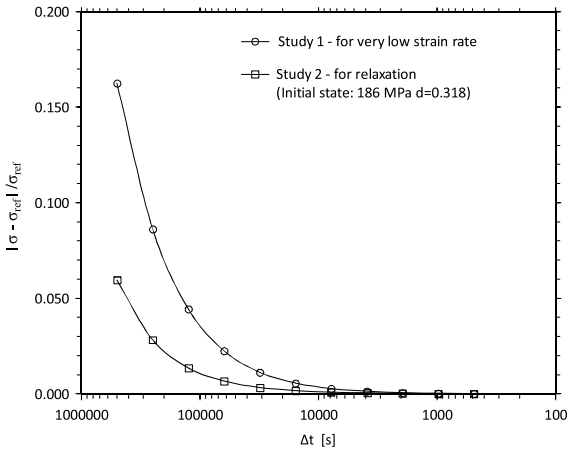

Fig. 7. Evaluation of stress convergence as a function of Δt. Study 1 — for very low strain rate ($\dot{\epsilon} = 5 \times 10^{-8}$ s^{-1}). Evaluated at $t = 6.7 \times 10^6$ s and with $\theta = 1$, $\gamma = 1$. Study 2 — for relaxation tests from the initial state: 186 MPa, $d = 0.318$. Evaluated at $t = 5 \times 10^6$ s and with $\theta = 1$, $\gamma = 1$. Total time for both tests $t = 10 \times 10^6$ s.

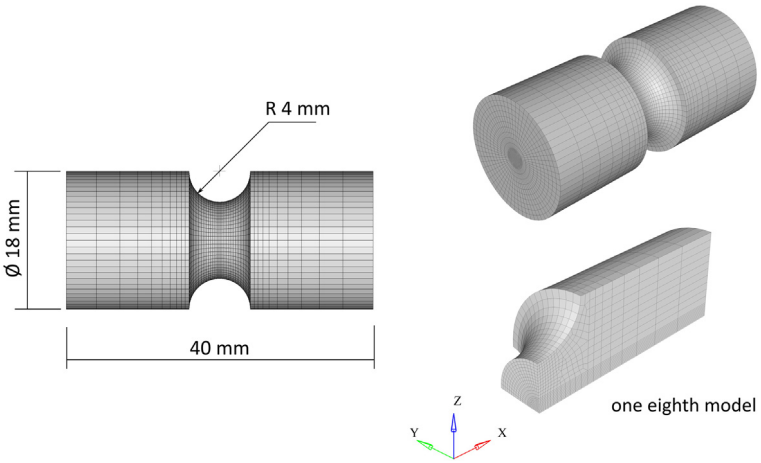

Fig. 8. Notched bar model.

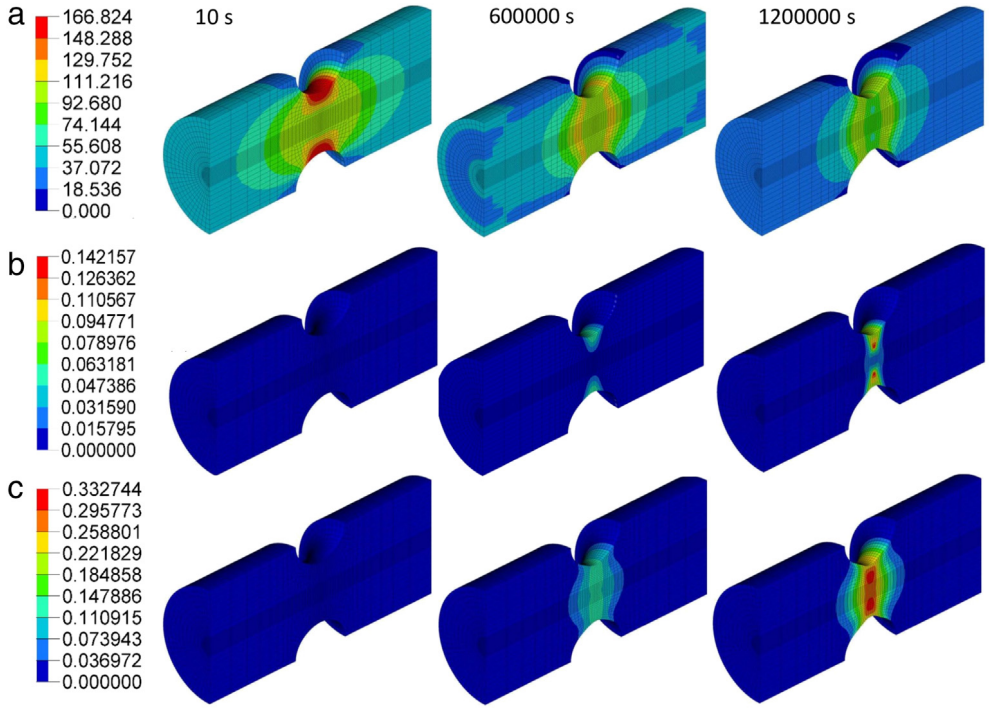

Fig. 9. Relaxation test on a notched bar. (a) von Mises stress [MPa], (b) evolution of plastic damage and (c) evolution of hydrolytic damage.

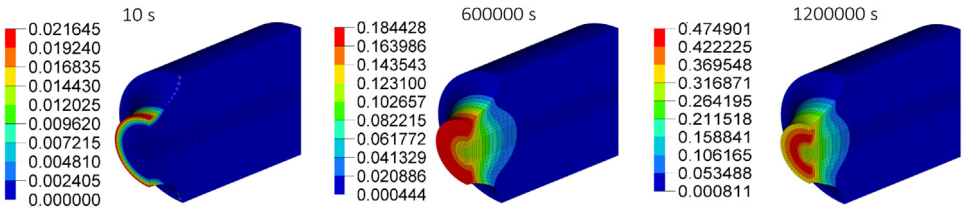

Fig. 10. Relaxation test on a notched bar. Evolution of the total damage.

4.3.1. Relaxation test

A prescribed displacement of $u_x = 1.2$ mm is linearly applied during 10 s, lengthening the specimen to 42.4 mm. After the bar has been stretched, the prescribed displacement is kept constant for 1.2×10^6 s ($\sim$14 days).

Fig. 9 shows the stress, plastic and hydrolytic damage fields (top to bottom), and how they evolve throughout the test (left to right). The hydrolytic damage becomes predominant, whereas plastic damage localizes. Similar to the behavior observed for ductile damage in metals [64,65], the maximum degradation starts on the exterior surface of the notch and evolves towards the center of the bar. Fig. 10 makes this observation clear, showing the evolution of the total damage. Additionally, the reaction load relaxation curves in Fig. 11 indicate the differences between the response for a specimen under hydrolytic degradation (continuous line) and another that is not (dashed line).

4.3.2. Creep test

In this second procedure, a total axial load of 8589.5 N was linearly applied in 10 s, and then kept constant until the end of the test ($t = 2.7 \times 10^6$ s, $\sim$31 days).

In such a condition, the specimen responded with a very low influence of viscoplastic creep effects, and a predominant contribution of hydrolytic degradation. Fig. 12 respectively shows the stress, plastic and hydrolytic damage fields (top to bottom), as well as how these fields evolve throughout the test (left to right). The evolution

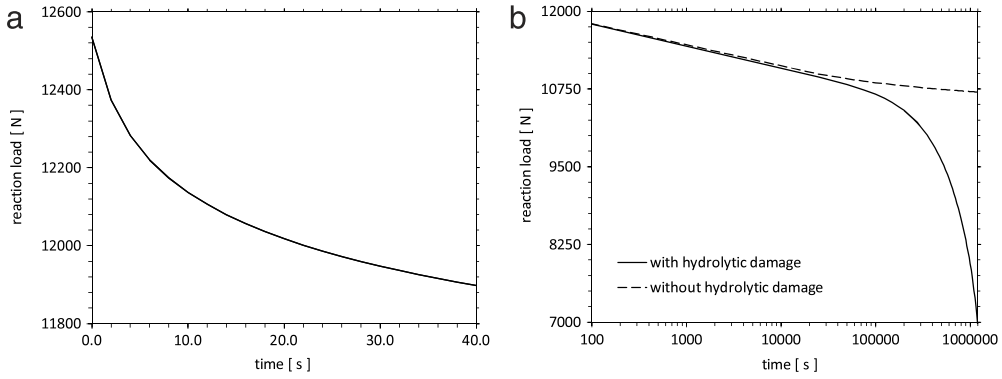

Fig. 11. Relaxation test on a notched bar. Initial and final relaxation, showing the distinct response of materials under hydrolysis effects or not.

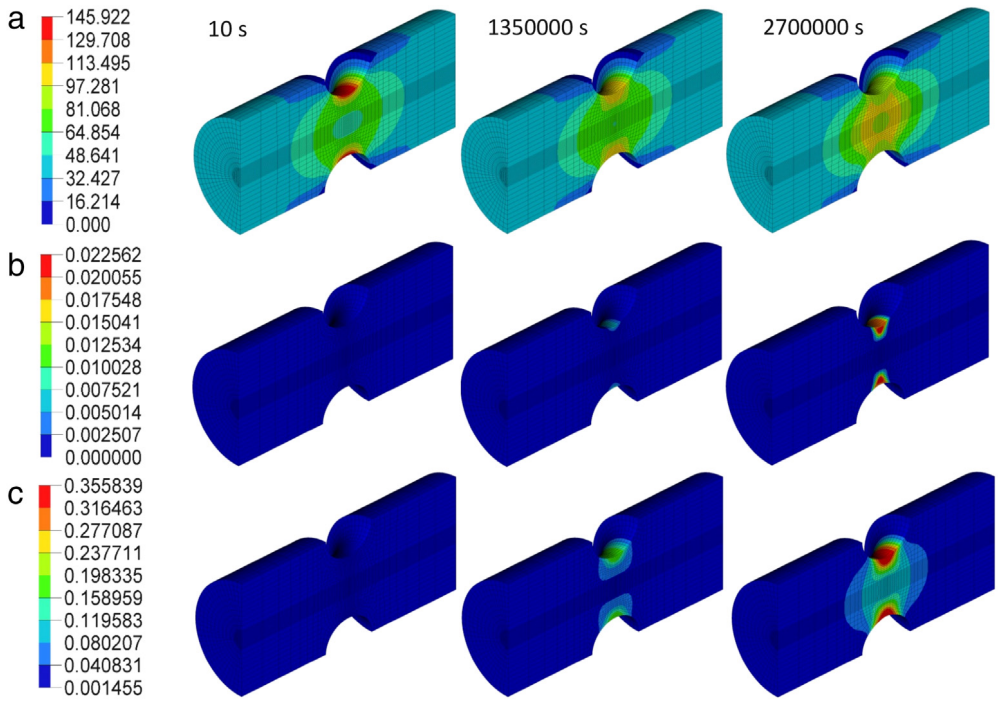

Fig. 12. Creep test on a notched bar. (a) von Mises stress [MPa], (b) evolution of plastic damage and (c) evolution of hydrolytic damage.

of the total damage can be observed in Fig. 13. Moreover, Fig. 14 displays what could be a typical situation involving the premature failure of a component subject to hydrolytic degradation, wherein the component undergoing hydrolysis is unable to withstand the load after a critical time.

4.3.3. Mesh sensitivity

Bearing in mind the local nature of the present damage formulation, a sensitivity analysis of von Mises stress and damage fields to mesh refinement was performed. To this end, the same relaxation test of Section 4.3.1, but now considering three differently refined meshes, was evaluated. Hexahedral elements (20-nodes, reduced integration) with average size of 1.0 mm (mesh 1), 0.5 mm (mesh 2) and 0.25 mm (mesh 3) were defined in the notch region (see Fig. 15).

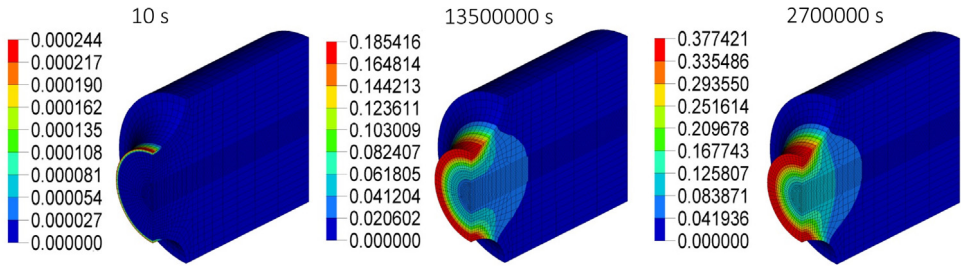

Fig. 13. Creep test on a notched bar. Total damage evolution.

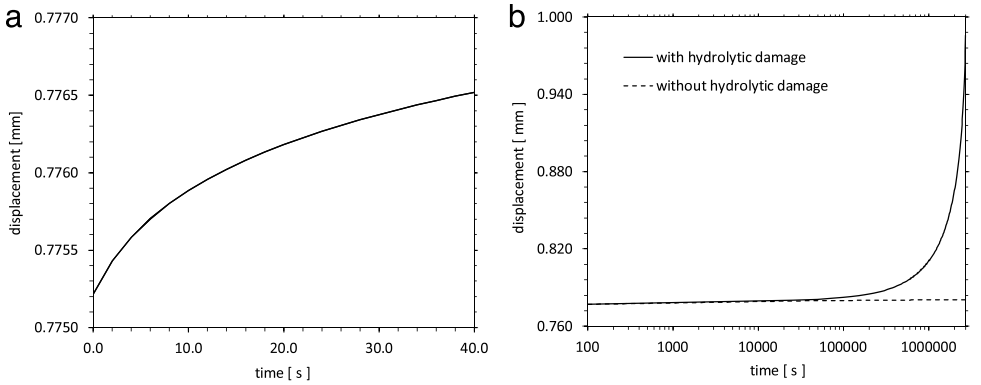

Fig. 14. Creep-like response of a material under hydrolytic degradation. Comparative results between a material that undergoes hydrolysis degradation and another that does not.

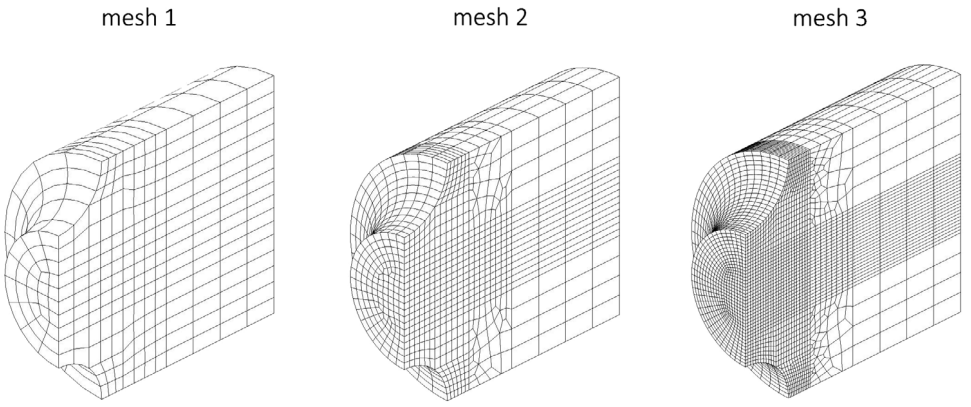

Fig. 15. Three different meshes used in the sensitivity analysis. Mesh 1 — element average size 1.00 mm. Mesh 2 — element average size 0.50 mm. Mesh 3 — element average size 0.25 mm.

Fig. 16 shows that as long as damage stays below 0.25 ($t = 8.28 \times 10^5$ s), differences lower than 10% are found among the results. However, once this damage value has been overcome, the solution for mesh 1 diverges from that of the two other refined meshes that yield, in turn, very similar results. This behavior is observed in Fig. 17 up to time $t = 1.200 \times 10^6$ s, the time that corresponds to the final state evaluated in Section 4.3.1. Allowing the solution to proceed from that point, localization effects take place and all results start to diverge, characterizing typical mesh-dependent solutions. As noticed in Fig. 18, when $t = 1.236 \times 10^6$ s, a maximum damage of 0.850 is achieved for the finest mesh and localization is clearly identified.

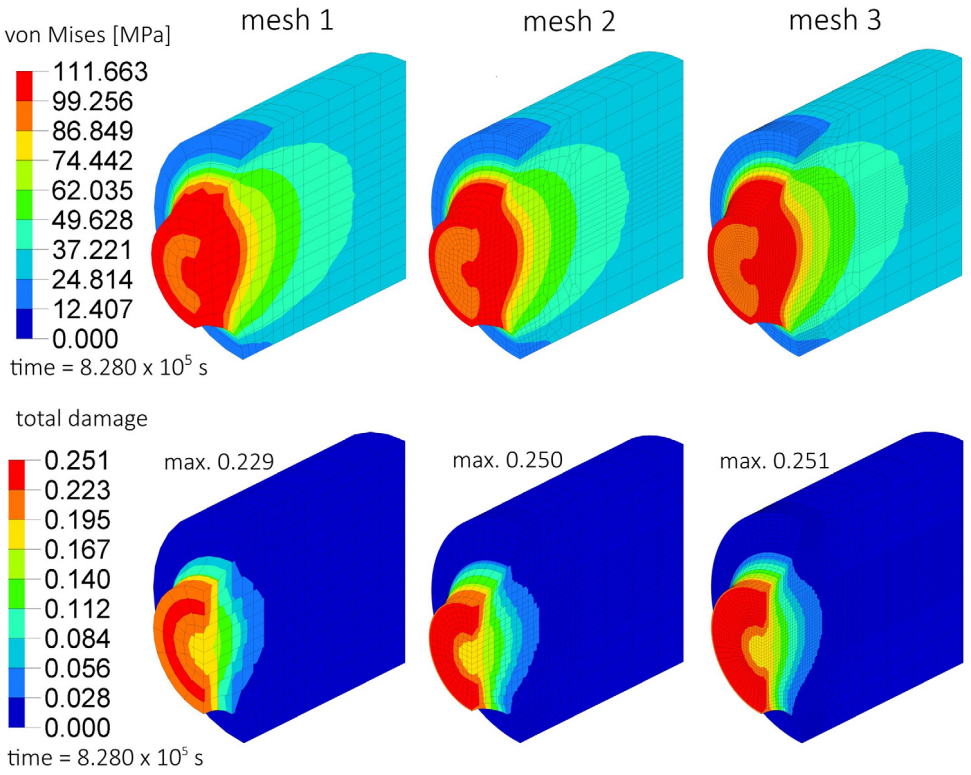

Fig. 16. Evaluation of von Mises [MPa] and total damage fields at $t = 8.280 \times 10^5$ s.

Fig. 19 shows how the mesh refinement influences the reaction load throughout relaxation. Logarithmic and linear scales for the same graph were used to better display initial and final stages of the process. All meshes present similar values at the initial stage, strongly dominated by viscous behavior. This pattern is kept up to $t = 8.28 \times 10^5$ s where, once again, the response of the coarsest mesh deviates from that of the finest ones. Up to the time $t = 1.200 \times 10^6$ s both refined meshes behave practically equal where localization is better identified in the finest mesh. It is worth mentioning that the results presented in Section 4.3.1 are in accordance with those shown here, being the mesh employed there comparable to mesh 3.

Some observations are valuable in the conclusion of this section. Results discussed above suggest that if a local approach is used, a critical damage value may be defined. If the damage field rests below this value, then low mesh dependency is expected [56]. Above this critical damage, which in the present cases could be estimated at $d \leq 0.45$ when $t = 1.200 \times 10^6$ s, a reliable solution is no longer assured. In such cases, regularization techniques like those proposed in [58–60] are mandatory.

4.4. Tests on a suture anchor

The development of bioabsorbable medical implants has taken place over the last decade resulting in several advances in medical procedures. The constitutive formulation established here can be a valuable tool in designing such components. Therefore, a simple demonstration of an analysis of a suture anchor is given (the reader interested in cases of suture anchors design may consult, for example, [66] and [67]).

To this objective, new values for the material parameters were identified in an attempt to reproduce the behavior of tensile and relaxation tests carried out on non-degraded and on nine-month degraded PLLA (poly-L-lactic acid) fibers [63]. The identification procedure was performed as follows. Assuming elastic compressible behavior (fixed Poisson's ratio $\nu = 0.410$), the elastic parameter μ was adjusted in order to reproduce the initial slope of the

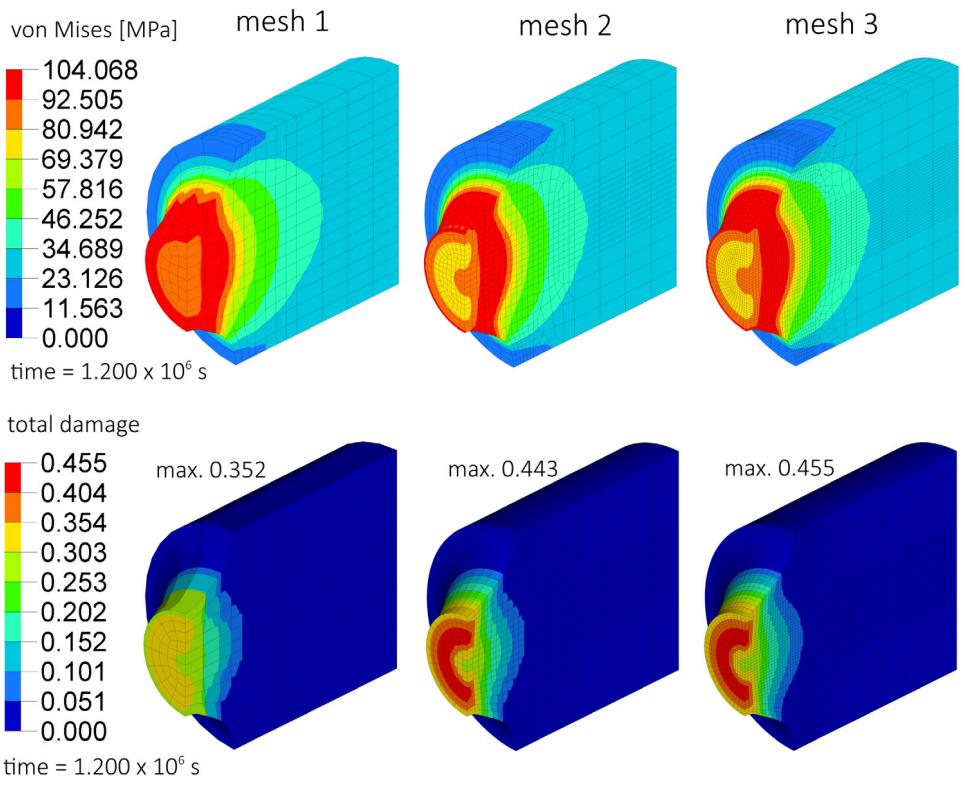

Fig. 17. Evaluation of von Mises [MPa] and total damage fields at $t = 1.200 \times 10^6$ s.

non-degraded tensile curve (isotropy was considered to calculate the bulk modulus K). Hardening and viscoplastic parameters were then estimated by fitting non-degraded tensile and relaxation curves. Since those experiments do not provide information on mechanical ductile damage, parameters that introduce only a small contribution of such a phenomenon were conveniently chosen (Table 2), making all the coupling effects possible to be evaluated into the simulation. Keeping all the previous parameters fixed, the hydrolytic constants were iteratively identified in order to reproduce the tensile test performed on two types of degraded fibers: those degraded under a zero load condition and those submitted to an axial load of 0.98 N [63]. This simple identification procedure led to the curve fitting shown in Fig. 20 and to the set of values presented in Table 2. These values should be considered as an illustrative example of the set of parameters necessary for running a representative simulation.

As indicated in Fig. 21, the suture anchor is considered partially inserted into a (rigid) foundation and a force is applied in its upper region perpendicularly to its longitudinal axis. The model is meshed with 10-node tetrahedral elements and a contact interface is defined in an area of transition between a fully clamped surface and the free surface. The model is submitted to a total load of 10 N in a rate of 1N s^{-1}, and then the load is kept constant until the end of the test (8×10^6 s, ∼92 days).

At $t = 8 \times 10^6$ s, the reference displacement that is initially $u_{\text{ref}} = 0.234$ mm reaches $u_{\text{ref}} = 1.488$ mm, mainly as an outcome of hydrolytic degradation. The von Mises stress distribution, as well as plastic, hydrolytic and total damage fields, are shown in Figs. 22 and 23. Additionally, for the sake of comparison, in Fig. 24 the displacement curve computed for a component subjected to hydrolytic degradation is shown simultaneously with another one for a material that does not undergo such an effect.

5. Conclusion

In this study, a constitutive model for elastic–viscoplastic materials subjected to ductile–hydrolytic damage was presented. The model satisfactorily succeeded in representing the coupling effects of inelastic flow, mechanical and

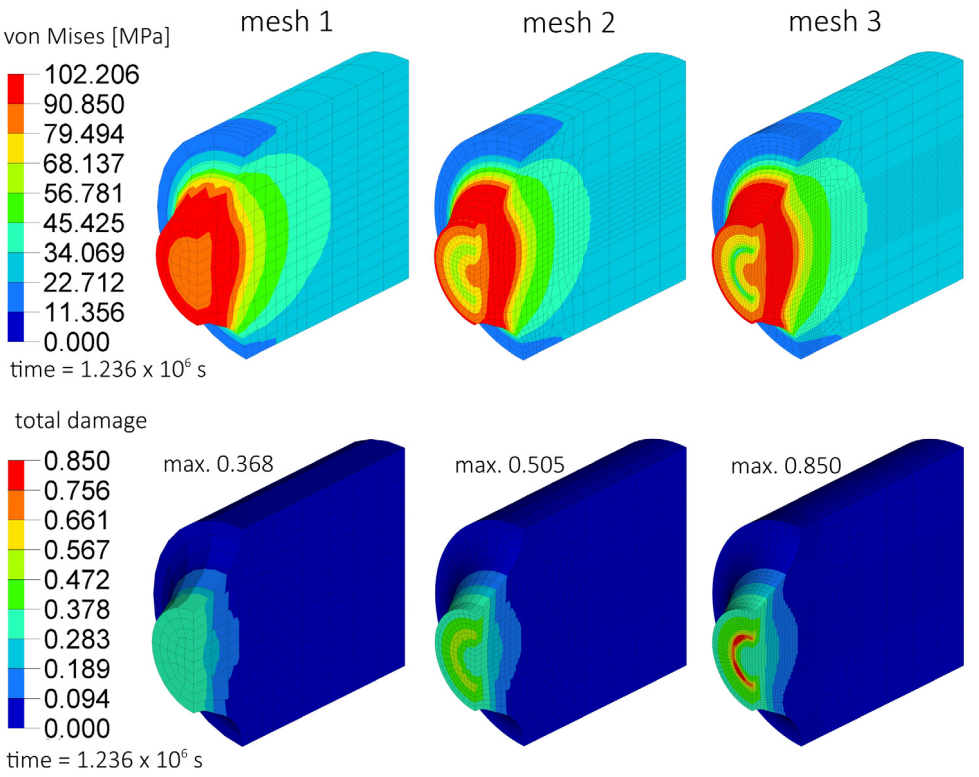

Fig. 18. Evaluation of von Mises [MPa] and total damage fields at $t = 1.236 \times 10^6$ s.

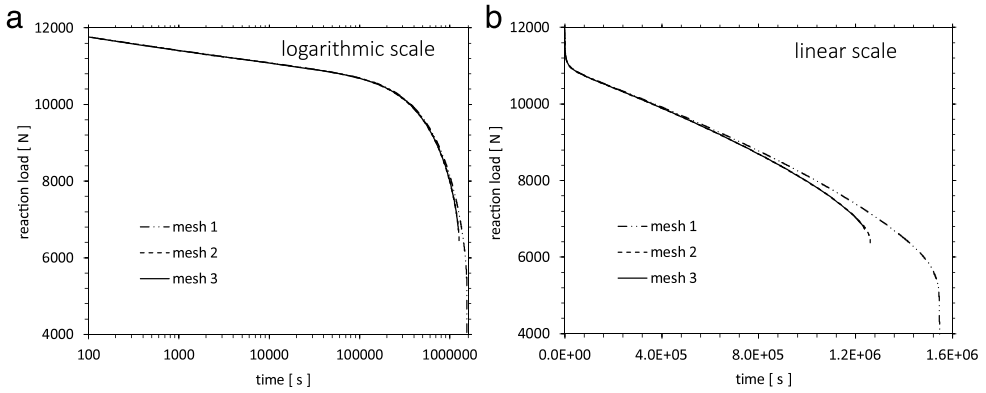

Fig. 19. Reaction load [N] curves associated with relaxation and degradation for three different mesh refinements. (a) Logarithmic scale. (b) Linear scale.

chemical induced damage. Despite the complexity of the phenomena involved, the update algorithm follows a simple operational scheme, being supported by a variational framework that provides sound thermodynamical consistency.

Some of the implications related to the dependence of dissipation functions on state variables, mainly those dependent on the elastic state, were analyzed by means of numerical experiments regarding $d^h_{n+\theta}$ and $Y_{n+\gamma}$. These experiments illustrate the possible effects such a dependence may cause in the solution of damage and stress.

As the current proposal is based on a local damage formulation, the model is susceptible to well-known drawbacks that such an approach may bring about. Some alternatives may be found in methods like the Thick Level Set (TLS)

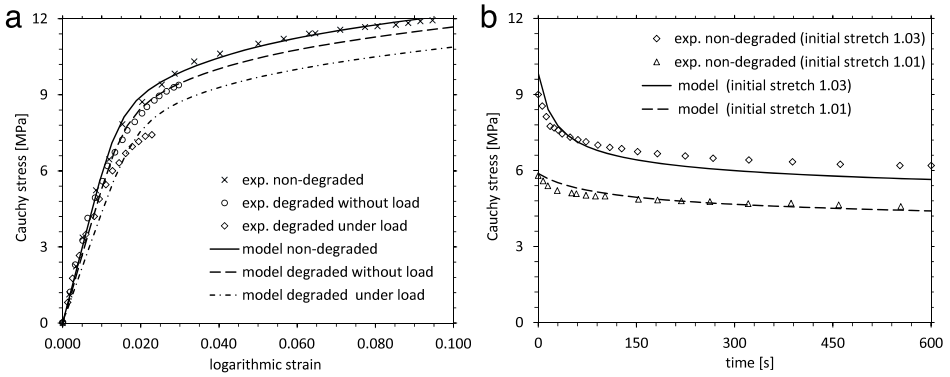

Fig. 20. Curve fitting of experimental data from [63] for PLLA. (a) Tensile test for non-degraded and degraded material. (b) Relaxation response for a non-degraded material.

Table 2
Constitutive material parameters identified from [63].

Material parameter	Symbol	Value
Shear modulus (MPa)	μ	211.2676
Bulk modulus (MPa)	K	1109.155
Linear isotropic hardening modulus (MPa)	k	2
Isotropic hardening modulus (MPa)	H	2
Isotropic hardening exponent	n	50
Yield stress (MPa)	σ_Y	2.3
Viscoplasticity exponent (rate sensitive)	η	0.188
Viscoplasticity constant (viscosity, 1/s)	c	0.008
Saturation function modulus (MPa)	h	27
Saturation function constant (MPa)	k_v	10
Plastic damage exponent	S	2
Plastic damage constant $(\mathrm{J/mm^3})^S$	N	8
Hydrolytic damage exponent	m	0.3742
Hydrolytic damage exponent (damage sensitivity)	n	1
Hydrolytic damage constant $(\mathrm{J/mm^3})^{\mathrm{m}}$	R	7999.636×10^3
Hydrolytic damage constant $(\mathrm{J/mm^3})$	g	1.46×10^{-4}

[58–60,68] or non-local formulations [14,57]. Those options may be explored in the future in order to deal with this specific issue.

Although some important experimental data are available in the literature for bioabsorbable materials, there still exists a lack of correlation of that data and their applicability to finite element simulations. Therefore, new efforts are required looking into the design of physical experiments and numerical models that should be mutually complementary.

The proposed material model was successfully implemented in two codes: an in-house code for finite kinematics called *CEOS* and the commercial code ABAQUS throughout UMAT routines. Simulations provided identical results in comparison tests run with the same element formulation in both codes.

Finally, examples based on three-dimensional finite element models highlight the potentialities of the current formulation to provide relevant information for engineering decisions in terms of product design and application.

Acknowledgement

The authors would like to thank the Brazilian “Conselho Nacional de Desenvolvimento Científico e Tecnológico - CNPq” (grant numbers: 157595/2012-9, 150531/2017-6, 309686/2013-0) for supporting this research.

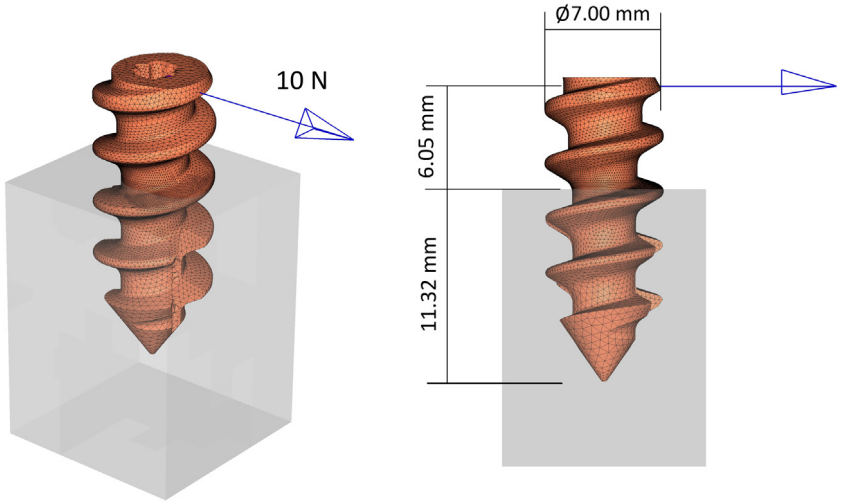

Fig. 21. Suture anchor geometry and finite element model.

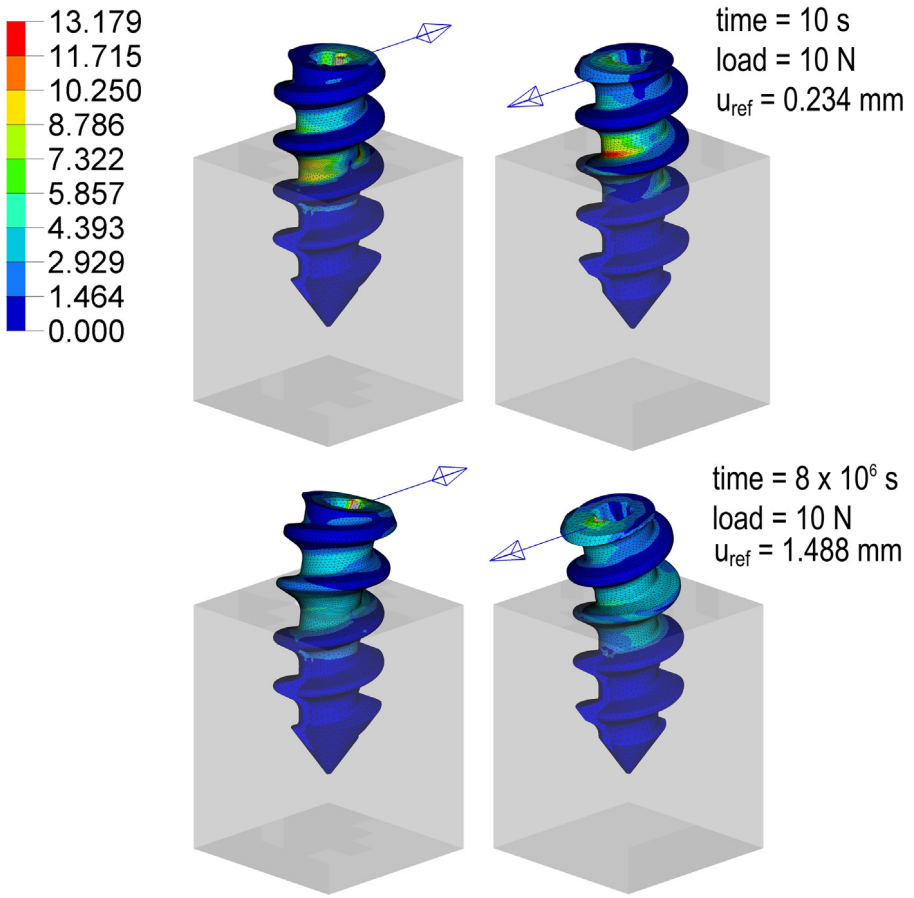

Fig. 22. von Mises stress in a creep test on a suture anchor.

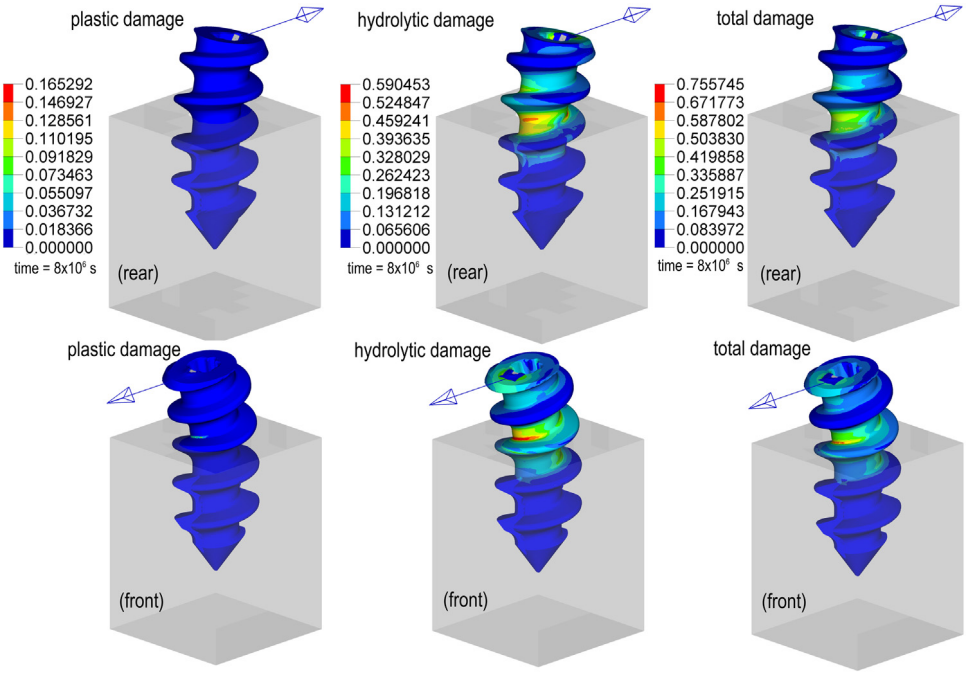

Fig. 23. Creep test on a suture anchor. Final damage state (8×10^6 s, ∼92 days).

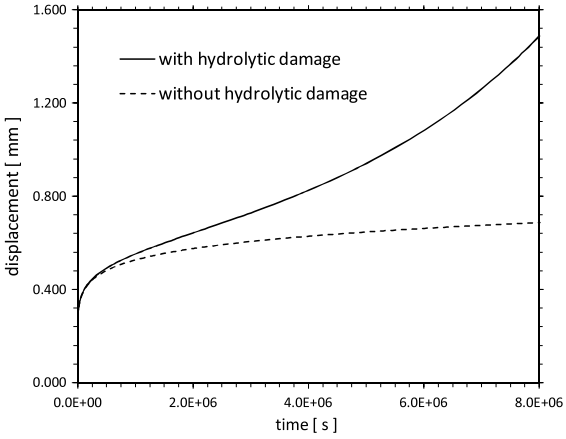

Fig. 24. Displacement vs. time for a device undergoing hydrolytic degradation and another that is not under degradation effects.

Appendix A. Incremental potential

Given the definitions (23), (24) and (27), the pseudo-potential (29) can be written as

$$\mathcal{P} = \dot{W} + (1-d)\,\sigma_Y \dot{\alpha} + \frac{c f_A(\alpha)}{\eta+1}\left(\frac{\dot{\alpha}}{c}\right)^{\eta+1} + Y\dot{d}^p + \frac{R}{2(1-d)^n (Y+g)^{m-1}}\left(\dot{d}^h\right)^2 - g\dot{d}\,. \tag{A.1}$$

An incremental counterpart of such function is devised as an approximate integral of the type

$$\mathcal{W} = \Delta W + \Delta t \phi^* \simeq \int_{t_n}^{t_{n+1}} \mathcal{P}\, dt, \tag{A.2}$$

that, by considering $\Delta W = (1 - d_{n+1})\, \tilde{W}_{n+1} - (1 - d_n)\, \tilde{W}_n$, $Y_{n+1} \equiv \tilde{W}_{n+1}$ and $Y_n \equiv \tilde{W}_n$, takes the final form

$$\begin{aligned}\mathcal{W} = {} & (1 - d_{n+1})\, Y_{n+1} - (1 - d_n)\, Y_n \\ & + \Delta t \left[(1 - d_{n+1})\, \sigma_Y \left(\frac{\Delta \alpha}{\Delta t} \right) + \frac{\mathsf{c} f_A(\alpha_{n+1})}{\eta + 1} \left(\frac{\Delta \alpha / \Delta t}{\mathsf{c}} \right)^{\eta+1} \right] \\ & + \Delta t \left[Y_{n+1} \frac{\Delta d^p}{\Delta t} \right] \\ & + \Delta t \left[\frac{R}{2(1 - d_{n+\theta})^n \left(Y_{n+\gamma} + g \right)^{m-1}} \left(\frac{\Delta d^h}{\Delta t} \right)^2 - g \frac{\Delta d^h}{\Delta t} \right] . \end{aligned} \tag{A.3}$$

One should notice that some state variables within the dissipation functions were chosen to take a full implicit value (i.e. $Y_{n+1}, \alpha_{n+1}, d_{n+1}$) while others assume intermediate values within the time interval $[t_n, t_{n+1}]$. The state variable $Y_{n+\gamma}$ in the last term of (A.3) is defined by the linearized function

$$Y_{n+\gamma} = \gamma Y_{n+1} + (1 - \gamma)\, Y_n\,, \qquad \gamma \in [0, 1]\,, \tag{A.4}$$

while the total damage $d_{n+\theta}$ is defined by the expression

$$d_{n+\theta} = d_n + \theta \left(\Delta \alpha \frac{(Y_{n+\theta})^S}{N} + \Delta d^h \right) , \qquad \theta \in [0, 1], \tag{A.5}$$

with $Y_{n+\theta}$ following (A.4) with the parameter $\theta \in [0, 1]$.

As already pointed out, the choice of these intermediate values and corresponding approximations is a matter of modeling and numerical convenience. A sensitivity analysis to integration parameters θ and γ was performed within the numerical tests.

Appendix B. Stationary conditions with respect to M

The minimization problem (30) must satisfy the constraints (20) on $\mathbf{M}$. Thus, optimality conditions with respect to this variable are set up by means of the Lagrangian:

$$\mathcal{L} = \mathcal{P} + \lambda_1 (\mathbf{M} : \mathbf{I}) + \lambda_2 (\mathbf{M} : \mathbf{M} - {}^3\!/_2)\,, \tag{B.1}$$

$$\frac{\partial \mathcal{L}}{\partial \mathbf{M}} : \delta \mathbf{M} = 0, \qquad \frac{\partial \mathcal{L}}{\partial \lambda_1} \delta \lambda_1 = 0, \qquad \frac{\partial \mathcal{L}}{\partial \lambda_2} \delta \lambda_2 = 0. \tag{B.2}$$

Using the first condition $\frac{\partial \mathcal{L}}{\partial \mathbf{M}} : \delta \mathbf{M} = 0$, and chosing $\delta \mathbf{M} = \mathbf{I}$ and $\delta \mathbf{M} = \mathbf{M}$, the Lagrangian multipliers become defined by:

$$\lambda_1 = \frac{1}{3} \frac{\partial \mathcal{P}}{\partial \mathbf{M}} : \mathbf{I}\,, \qquad \lambda_2 = \frac{1}{3} \frac{\partial \mathcal{P}}{\partial \mathbf{M}} : \mathbf{M}\,. \tag{B.3}$$

Replacing (B.3) into ((B.2)-a) leads to

$$\frac{\partial \mathcal{L}}{\partial \mathbf{M}} : \delta \mathbf{M} = \frac{\partial \mathcal{P}}{\partial \mathbf{M}} : \delta \mathbf{M} + \left[\left(\frac{1}{3} \frac{\partial \mathcal{P}}{\partial \mathbf{M}} : \mathbf{I} \right) \mathbf{I} + \left(\frac{2}{3} \frac{\partial \mathcal{P}}{\partial \mathbf{M}} : \mathbf{M} \right) \mathbf{M} \right] : \delta \mathbf{M} = 0. \tag{B.4}$$

In order to evaluate $\frac{\partial \mathcal{P}}{\partial \mathbf{M}} : \delta \mathbf{M}$, let the time derivative of W be written as

$$\dot{W} = (1 - d) \left[\tilde{\mathbf{P}} : \dot{\mathbf{F}} + \tilde{\boldsymbol{\chi}} : \dot{\mathbf{F}}^p + \tilde{\kappa} \dot{\alpha} \right] - Y \dot{d}^p - Y \dot{d}^h\,, \tag{B.5}$$

where

$$\tilde{\boldsymbol{\chi}} = \frac{\partial \tilde{W}}{\partial \mathbf{F}^p} = -\mathbf{C}^e \mathbf{S}^e \mathbf{F}^{p\,-T} = -\tilde{\boldsymbol{\Sigma}}^e \mathbf{F}^{p\,-T}\,, \tag{B.6}$$

and $\dot{\mathbf{F}}^p = \mathbf{D}^p \mathbf{F}^p$, $\mathbf{D}^p = \dot{\alpha} \mathbf{M}$.

After some tensor algebra, it follows that

$$\frac{\partial \mathcal{P}}{\partial \mathbf{M}} : \delta\mathbf{M} = -(1-d)\left[\dot{\alpha}\mathbf{I}\left(\tilde{\boldsymbol{\Sigma}}^e \mathbf{F}^{p\,-T}\right)\mathbf{F}^{p\,T}\right] : \mathbb{I}_s : \delta\boldsymbol{M} = -(1-d)\,\dot{\alpha}\tilde{\boldsymbol{\Sigma}}^e : \delta\mathbf{M}, \tag{B.7}$$

where $\mathbb{I}_s$ is the fourth order symmetric identity tensor. Replacing this result into (B.4) and operating terms yields

$$\frac{\partial \mathcal{L}}{\partial \mathbf{M}} = -\tilde{\boldsymbol{\Sigma}}^e_d + \frac{2}{3}\left(\tilde{\boldsymbol{\Sigma}}^e_d : \mathbf{M}\right)\mathbf{M} = 0 \text{ and } \mathbf{M} = \sqrt{\frac{3}{2}}\frac{\tilde{\boldsymbol{\Sigma}}^e_d}{\left\|\tilde{\boldsymbol{\Sigma}}^e_d\right\|}, \tag{B.8}$$

where $\tilde{\Sigma}^e_d$ is the effective deviatoric Mandel stress.

Analogous procedure is used for the incremental problem. In this case, it is considered the incremental Lagrangian function

$$\mathcal{L}_\Delta = \mathcal{W} + \lambda_1(\mathbf{M} : \mathbf{I}) + \lambda_2(\mathbf{M} : \mathbf{M} - {}^3\!/_2)\,, \tag{B.9}$$

$$\mathcal{W} = (1-d_{n+1})\,Y_{n+1} - (1-d_n)\,Y_n + \Delta t\phi^*. \tag{B.10}$$

By evaluating the first term of the stationarity condition $\frac{\partial \mathcal{L}_\Delta}{\partial \mathbf{M}} : \delta\mathbf{M} = 0$, this leads to

$$\frac{\partial \mathcal{W}}{\partial \mathbf{M}} : \delta\mathbf{M} = \frac{\partial\,(1-d_{n+1})\,Y_{n+1}}{\partial \mathbf{M}} : \delta\mathbf{M} + \Delta t\frac{\partial \phi^*}{\partial \mathbf{M}} : \delta\mathbf{M}, \tag{B.11}$$

which after a lengthy procedure can be written in a compact form as

$$\frac{\partial \mathcal{W}}{\partial \mathbf{M}} : \delta\mathbf{M} = \mathtt{K}\frac{\partial Y_{n+1}}{\partial \mathbf{M}} : \delta\mathbf{M}, \tag{B.12}$$

where $\mathtt{K}$ is a scalar quantity. Using the same procedure presented before, it turns out that

$$\lambda_1 = \frac{1}{3}\mathtt{K}\frac{\partial Y_{n+1}}{\partial \mathbf{M}} : \mathbf{I}, \qquad \lambda_2 = \frac{1}{3}\mathtt{K}\frac{\partial Y_{n+1}}{\partial \mathbf{M}} : \mathbf{M}. \tag{B.13}$$

In order to evaluate $\frac{\partial Y_{n+1}}{\partial \mathbf{M}}$, the isochoric free energy W^e_{n+1} is assumed here to have a Hencky-like form

$$W^e_{n+1} = \frac{1}{2}\hat{\boldsymbol{\varepsilon}}^e_{n+1} : \mathbb{D} : \hat{\boldsymbol{\varepsilon}}^e_{n+1}\,, \tag{B.14}$$

where $\hat{\boldsymbol{\varepsilon}}^e_{n+1} = \hat{\boldsymbol{\varepsilon}}^{pr}_{n+1} - \Delta\alpha\mathbf{M}$ is the isochoric contribution of the logarithmic strain. Thus,

$$\frac{\partial Y_{n+1}}{\partial \mathbf{M}} = \frac{\partial W^e_{n+1}}{\partial \mathbf{M}} = -\Delta\alpha\tilde{\boldsymbol{\Sigma}}^e_{d\,n+1}, \tag{B.15}$$

in which $\tilde{\boldsymbol{\Sigma}}_{d\,n+1} = \tilde{\boldsymbol{\Sigma}}^{pr}_{d\,n+1} - 2\mu\Delta\alpha\mathbf{M}$, $\tilde{\boldsymbol{\Sigma}}^{pr}_{d\,n+1} = 2\mu\hat{\boldsymbol{\varepsilon}}^{pr}_{n+1}$ is the definition of the isochoric elastic Mandel stress, and μ is the material shear modulus. Replacing (B.15) into (B.12) an explicit form for $\mathbf{M}$ is finally obtained:

$$\frac{\partial \mathcal{L}_\Delta}{\partial \mathbf{M}} = -\tilde{\boldsymbol{\Sigma}}_{d\,n+1} + \frac{2}{3}\left[\tilde{\boldsymbol{\Sigma}}_{d\,n+1} : \mathbf{M}\right]\mathbf{M} = 0, \qquad \boldsymbol{M} = \sqrt{\frac{3}{2}}\frac{\tilde{\boldsymbol{\Sigma}}_{d\,n+1}}{\left\|\tilde{\boldsymbol{\Sigma}}_{d\,n+1}\right\|}. \tag{B.16}$$

Additionally, as a consequence of using a Hencky-like potential, the substitution of $\mathbf{M}$ into the definition of the deviatoric Mandel stress $\tilde{\boldsymbol{\Sigma}}_{d\,n+1}$ shows that $\tilde{\boldsymbol{\Sigma}}_{d\,n+1}$ and $\tilde{\boldsymbol{\Sigma}}^{pr}_{d\,n+1}$ are colinear, making it possible to compute $\mathbf{M}$ in terms of predictor tensors:

$$\mathbf{M} = \sqrt{\frac{3}{2}}\frac{\tilde{\boldsymbol{\Sigma}}^{pr}_{d\,n+1}}{\left\|\tilde{\boldsymbol{\Sigma}}^{pr}_{d\,n+1}\right\|} = \sqrt{\frac{3}{2}}\frac{\hat{\mathbf{C}}^{pr}_{n+1}}{\left\|\hat{\mathbf{C}}^{pr}_{n+1}\right\|}. \tag{B.17}$$

Appendix C. Stationary conditions with respect to $\dot{\alpha}$ and $\Delta\alpha$

The stationary condition of $\mathcal{P}$ with respect to $\dot{\alpha}$ can be evaluated in a straightforward manner by means of

$$\frac{\partial \mathcal{P}}{\partial \dot{\alpha}}\delta\dot{\alpha} = \left[\frac{\partial \dot{W}}{\partial \dot{\alpha}} + \frac{\partial}{\partial \dot{\alpha}}\left((1-d)\sigma_Y\dot{\alpha} + \frac{\mathtt{c}\,f_A(\alpha)}{\eta+1}\left(\frac{\dot{\alpha}}{\mathtt{c}}\right)^{\eta+1}\right) + Y\frac{\partial \dot{d}^p}{\partial \dot{\alpha}}\right]\delta\dot{\alpha} = 0. \tag{C.1}$$

Taking into account the time derivative of the free-energy potential $\dot{W}$ and (B.7), condition (C.1) can be expressed as

$$\frac{\partial \mathcal{P}}{\partial \dot{\alpha}} = (1-d)\left[\tilde{\chi} : \frac{\partial \dot{\mathbf{F}}^p}{\partial \dot{\alpha}} + \tilde{\kappa} + \sigma_Y\right] + f_A(\alpha)\left(\frac{\dot{\alpha}}{\mathsf{c}}\right)^{\eta} \tag{C.2}$$

$$= (1-d)\left[(\sigma_Y + \tilde{\kappa}) - \tilde{\Sigma}_{eq}\right] + f_A(\alpha)\left(\frac{\dot{\alpha}}{\mathsf{c}}\right)^{\eta} = 0, \tag{C.3}$$

where $\tilde{\Sigma}_{eq} = \tilde{\mathbf{\Sigma}}^e : \mathbf{M}$ is a von Mises-like effective stress.

Despite the simplicity of this derivation in the continuous framework, more elaborated expressions appear in the incremental counterpart due to the coupling effects produced by the increment $\Delta\alpha$ on the potential. The stationary condition of $\mathcal{W}$ with respect to $\Delta\alpha$ is formally written as

$$\frac{\partial \mathcal{W}}{\partial \Delta\alpha}\delta\Delta\alpha = \left[(1-d_{n+1})\,\frac{\partial Y_{n+1}}{\partial \Delta\alpha} - Y_{n+1}\frac{\partial d^p_{n+1}}{\partial \Delta\alpha} + \Delta t\,\frac{\partial \phi^*}{\partial \Delta\alpha}\right]\delta\Delta\alpha = 0. \tag{C.4}$$

In (C.4), the terms related to the dissipative functions are represented by

$$\Delta t\,\frac{\partial \phi^*}{\partial \Delta\alpha} = \Delta t\,\frac{\partial \psi^*_{vp}}{\partial \Delta\alpha} + \Delta t\,\frac{\partial \varphi^*_{dp}}{\partial \Delta\alpha} + \Delta t\,\frac{\partial \varphi^*_{dh}}{\partial \Delta\alpha}\,, \tag{C.5}$$

where the viscoplastic, ductile-damage and hydrolytic-damage contributions are respectively given by

$$\Delta t\,\frac{\partial \psi^*_{vp}}{\partial \Delta\alpha} = (1-d_{n+1})\,\sigma_Y + f_A(\alpha_{n+1})\left(\frac{\Delta\alpha/\Delta t}{\mathsf{c}}\right)^{\eta} + \Delta t\left[\frac{\mathsf{c}}{\eta+1}\left(\frac{\Delta\alpha/\Delta t}{\mathsf{c}}\right)^{\eta+1}\frac{\partial f_A(\alpha_{n+1})}{\partial \Delta\alpha} - \sigma_Y\left(\frac{\Delta\alpha}{\Delta t}\right)\frac{\partial d^p_{n+1}}{\partial \Delta\alpha}\right], \tag{C.6}$$

$$\Delta t\,\frac{\partial \varphi^*_{dp}}{\partial \Delta\alpha} = \Delta t\,\frac{Y^{S+1}_{n+1}}{N}\frac{1}{\Delta t} + \Delta t\,\frac{\Delta\alpha}{\Delta t}\,(S+1)\,\frac{Y^{S}_{n+1}}{N}\frac{\partial Y_{n+1}}{\partial \Delta\alpha}\,, \tag{C.7}$$

$$\Delta t\,\frac{\partial \varphi^*_{dh}}{\partial \Delta\alpha} = \Delta t\,\frac{R}{2}\left(\frac{\Delta d^h}{\Delta t}\right)^2\left[\begin{array}{c}\gamma\,\dfrac{1-m}{(1-d_{n+\theta})^n\left(Y_{n+\gamma}+g\right)^m}\dfrac{\partial Y_{n+1}}{\partial \Delta\alpha}\\ +\dfrac{n}{(1-d_{n+\theta})^{n+1}\left(Y_{n+\gamma}+g\right)^{m-1}}\dfrac{\partial d^p_{n+\theta}}{\partial \Delta\alpha}\end{array}\right]. \tag{C.8}$$

Finally, given the definition (A.5) for $d_{n+\theta}$, as well as the partial derivative of the ductile damage with respect to $\Delta\alpha$

$$\frac{\partial d^p_{n+\theta}}{\partial \Delta\alpha} = \theta\left(\frac{Y^S_{n+\theta}}{N} + \theta S\Delta\alpha\,\frac{Y^{S-1}_{n+\theta}}{N}\frac{\partial Y_{n+1}}{\partial \Delta\alpha}\right), \qquad \theta \in [0,1]\,, \tag{C.9}$$

condition (C.4) is written in a compact form as

$$\frac{\partial \mathcal{W}}{\partial \Delta\alpha} = \mathcal{G}\,\frac{\partial W^e_{n+1}}{\partial \Delta\alpha} + \mathtt{A} + \Delta t\,\mathtt{B} = 0, \tag{C.10}$$

being $\mathcal{G}$, $\mathtt{A}$, and $\mathtt{B}$ respectively defined by (51), (52) and (53).

Appendix D. Stationary conditions with respect to $\dot{d}^h$ and Δd^h

The stationary condition of $\mathcal{P}$ with respect to $\dot{d}^h$ results in

$$\frac{\partial \mathcal{P}}{\partial \dot{d}^h}\delta\dot{d}^h = \left[\frac{\partial \dot{W}}{\partial \dot{d}^h} + \frac{\partial}{\partial \dot{d}^h}\left(\frac{R}{2\left(1-d^h\right)^n(Y+g)^{m-1}}\,\dot{d}^{h\,2} - g\dot{d}^h\right)\right]\delta\dot{d}^h = 0, \tag{D.1}$$

which once rearranged gives the evolution equation for the hydrolytic damage (26), repeated here for convenience:

$$\dot{d}^h = (1-d)^n\,\frac{(Y+g)^m}{R}\,. \tag{D.2}$$

Once again, this straightforward derivation of the continuum case becomes lengthier in its incremental counterpart due to the couplings produced by Δd^h on $\mathcal{W}$ (expressions (37) and (39)):

$$\frac{\partial \mathcal{W}}{\partial \Delta d^h}\delta\Delta d^h = \left[\frac{\partial}{\partial \Delta d^h}\left[(1-d_{n+1})\,Y_{n+1}\right] + \Delta t\left(\frac{\partial \psi^*_{vp}}{\partial \Delta d^h} + \frac{\partial \varphi^*_{dh}}{\partial \Delta d^h}\right)\right]\delta\Delta d^h \tag{D.3}$$

$$= -Y_{n+1} - \Delta t\sigma_Y\left(\frac{\Delta\alpha}{\Delta t}\right) + \frac{\partial \varphi^*_{dh}}{\partial \dot{d}^h} + \theta\Delta t\frac{\partial \varphi^*_{dh}}{\partial d^h_{n+\theta}} = 0, \tag{D.4}$$

where

$$\frac{\partial \varphi^*_{dh}}{\partial \dot{d}^h} = \frac{R}{(1-d_{n+\theta})^n\left(Y_{n+\gamma}+g\right)^{m-1}}\frac{\Delta d^h}{\Delta t} - g, \tag{D.5}$$

$$\frac{\partial \varphi^*_{dh}}{\partial d^h_{n+\theta}} = \frac{n}{2(1-d_{n+\theta})^{n+1}}\frac{R}{\left(Y_{n+\gamma}+g\right)^{m-1}}\left(\frac{\Delta d^h}{\Delta t}\right)^2. \tag{D.6}$$

Finally, replacing (D.5) and (D.6) into (D.4) yields

$$r_2 = \frac{\partial \mathcal{W}}{\partial \Delta d^h} = -\left(Y_{n+1}+g\right) + \frac{R}{(1-d_{n+\theta})^n\left(Y_{n+\gamma}+g\right)^{m-1}}\frac{\Delta d^h}{\Delta t} + \Delta t\left[\theta\frac{nR}{2(1-d_{n+\theta})^{n+1}\left(Y_{n+\gamma}+g\right)^{m-1}}\left(\frac{\Delta d^h}{\Delta t}\right)^2 - \sigma_Y\left(\frac{\Delta\alpha}{\Delta t}\right)\right] = 0. \tag{D.7}$$

Appendix E. The second Piola–Kirchhoff: Incremental form

In what follows, it is shown that the stress update described in terms of the second Piola–Kirchhoff stress can be evaluated by considering (54), that is

$$\mathbf{S}_{n+1} = 2\frac{\partial \mathcal{W}}{\partial \mathbf{C}_{n+1}}, \tag{E.1}$$

where

$$\frac{\partial \mathcal{W}}{\partial \mathbf{C}_{n+1}} = (1-d_{n+1})\frac{\partial Y_{n+1}}{\partial \mathbf{C}_{n+1}} - Y_{n+1}\frac{\partial d^p_{n+1}}{\partial \mathbf{C}_{n+1}} + \Delta t\frac{\partial \phi^*}{\partial \mathbf{C}_{n+1}}, \tag{E.2}$$

and

$$\Delta t\frac{\partial \phi^*}{\partial \mathbf{C}_{n+1}} = \Delta t\frac{\partial \psi^*_{vp}}{\partial \mathbf{C}_{n+1}} + \Delta t\frac{\partial \varphi^*_{dp}}{\partial \mathbf{C}_{n+1}} + \Delta t\frac{\partial \varphi^*_{dh}}{\partial \mathbf{C}_{n+1}}. \tag{E.3}$$

Each term of (E.3) is respectively given by

$$\Delta t\frac{\partial \psi^*_{vp}}{\partial \mathbf{C}_{n+1}} = -\Delta t\sigma_Y\left(\frac{\Delta\alpha}{\Delta t}\right)\frac{\partial d^p_{n+1}}{\partial \mathbf{C}_{n+1}}, \tag{E.4}$$

$$\Delta t\frac{\partial \varphi^*_{dp}}{\partial \mathbf{C}_{n+1}} = \Delta t\frac{\Delta\alpha}{\Delta t}(S+1)\frac{Y^S_{n+1}}{N}\frac{\partial Y_{n+1}}{\partial \mathbf{C}_{n+1}}, \tag{E.5}$$

and

$$\Delta t\frac{\partial \varphi^*_{dh}}{\partial \mathbf{C}_{n+1}} = \Delta t\frac{R}{2}\left(\frac{\Delta d^h}{\Delta t}\right)^2\left[\theta\frac{n}{(1-d_{n+\theta})^{n+1}\left(Y_{n+\gamma}+g\right)^{m-1}}\theta S\Delta\alpha\frac{Y^{S-1}_{n+\theta}}{N}\frac{\partial Y_{n+1}}{\partial \mathbf{C}_{n+1}} + \gamma\frac{1-m}{(1-d_{n+\theta})^n\left(Y_{n+\gamma}+g\right)^m}\frac{\partial Y_{n+1}}{\partial \mathbf{C}_{n+1}}\right]. \tag{E.6}$$

Replacing (E.4), (E.5) and (E.6) into (E.3), and (E.3) into (E.2) the second Piola–Kirchhoff stress takes the form of the expression (54), that is

$$\mathbf{S}_{n+1} = 2\frac{\partial \bar{\mathcal{W}}}{\partial \mathbf{C}_{n+1}} \equiv 2\frac{\partial \mathcal{W}}{\partial \mathbf{C}_{n+1}} = \mathcal{G}\tilde{\mathbf{S}}_{n+1}. \tag{E.7}$$

References

[1] K. Rajagopal, A. Srinivasa, A. Wineman, On the shear and bending of a degrading polymer beam, Int. J. Plast. 23 (9) (2007) 1618–1636.
[2] J.S. Soares, J.E.J. Moore, K.R. Rajagopal, Constitutive framework for biodegradable polymers with applications to biodegradable stents, ASAIO J. 54 (3) (2008) 295–301.
[3] J. Soares, K. Rajagopal, J. Moore, Deformation-induced hydrolysis of a degradable polymeric cylindrical annulus, Biomech. Model. Mechanobiol. 9 (2010) 177–186.
[4] A. Vieira, A. Marques, R. Guedes, V. Tita, Material model proposal for biodegradable materials, in: 11th International Conference on the Mechanical Behavior of Materials, Procedia Eng. 10 (2011) 1597–1602.
[5] A.C. Vieira, R.M. Guedes, V. Tita, Constitutive models for biodegradable thermoplastic ropes for ligament repair, Compos. Struct. 94 (11) (2012) 3149–3159.
[6] K. Khan, T. El-Sayed, A phenomenological constitutive model for the nonlinear viscoelastic responses of biodegradable polymers, Acta Mech. 224 (2) (2013) 287–305.
[7] A.C. Vieira, R.M. Guedes, V. Tita, Constitutive modeling of biodegradable polymers: Hydrolytic degradation and time-dependent behavior, Int. J. Solids Struct. 51 (5) (2014) 1164–1174.
[8] S. Baek, T.J. Pence, On mechanically induced degradation of fiber-reinforced hyperelastic materials, Math. Mech. Solids 16 (4) (2011) 406–434.
[9] Y. Wang, J. Pan, X. Han, C. Sinka, L. Ding, A phenomenological model for the degradation of biodegradable polymers, Biomaterials 29 (23) (2008) 3393–3401.
[10] K.R. Rajagopal, A. Muliana, Shear deformation of a non-linear solid undergoing deterioration of material properties, Int. J. Struct. Changes Solids 1 (1) (2009) 1–19.
[11] A. Muliana, K. Rajagopal, Modeling the response of nonlinear viscoelastic biodegradable polymeric stents, Int. J. Solids Struct. 49 (7–8) (2012) 989–1000.
[12] E.A. Fancello, L.P. Lindenmeyer, C.R. Roesler, G.V. Salmória, A simple extension of Lemaitre's elastoplastic damage model to account for hydrolytic degradation, Lat. Am. J. Solids Struct. 11 (5) (2014) 884–906.
[13] J. Lemaitre, A Course on Damage Mechanics, second ed., Springer-Verlag, 1996.
[14] J. Lemaitre, R. Desmorat, Engineering Damage Mechanics: Ductile, Creep, Fatigue and Brittle Failures, Springer-Verlag, 2005.
[15] J. Bergstrom, D. Hayman, An overview of mechanical properties and material modeling of polylactide (PLA) for medical applications, Ann. Biomed. Eng. (2015) 1–11.
[16] A. Bobel, S. Petisco, J. Sarasua, W. Wang, P. McHugh, Computational bench testing to evaluate the short-term mechanical performance of a polymeric stent, Cardiovasc. Eng. Technol. 6 (4) (2015) 519–532.
[17] E. Boland, R. Shine, N. Kelly, C. Sweeney, P. McHugh, A review of material degradation modelling for the analysis and design of bioabsorbable stents, Ann. Biomed. Eng. (2015) 1–16.
[18] J.S. Soares, James E.J. Moore, Biomechanical challenges to polymeric biodegradable stents, Ann. Biomed. Eng. (2015) 1–20.
[19] I. Bastos, J. Vasconcellos, J. Gomes, H.S. Costa-Mattos, A continuum damage model for the stress corrosion cracking of austenitic stainless steel, J. Braz. Soc. Mech. Sci. Eng. 27 (2) (2005) 186–191.
[20] H.S. Costa-Mattos, I.N. Bastos, J.A.C.P. Gomes, A simple model for slow strain rate and constant load corrosion tests of austenitic stainless steel in acid aqueous solution containing sodium chloride, Corros. Sci. 50 (10) (2008) 2858–2866.
[21] D. Gastaldi, V. Sassi, L. Petrini, M. Vedani, S. Trasatti, F. Migliavacca, Continuum damage model for bioresorbable magnesium alloy devices - Application to coronary stents, J. Mech. Behav. Biomed. Mater. 4 (3) (2011) 352–365.
[22] J.A. Grogan, B.J. O'Brien, S.B. Leen, P.E. McHugh, A corrosion model for bioabsorbable metallic stents, Acta Biomater. 7 (9) (2011) 3523–3533.
[23] H.S. Costa-Mattos, I.N. Bastos, J. A.C.P. Gomes, A thermodynamically consistent modelling of stress corrosion tests in elasto-viscoplastic materials, Corros. Sci. 80 (2014) 143–153.
[24] N. Miller, D. Williams, The in vivo and in vitro degradation of poly(glycolic acid) suture material as a function of applied strain, Biomaterials 5 (6) (1984) 365–368.
[25] D. Hayman, C. Bergerson, S. Miller, M. Moreno, J.E. Moore, The effect of static and dynamic loading on degradation of PLLA stent fibers, J. Biomech. Eng. 136 (8) (2014) 081006.1–081006.9.
[26] C. Roesler, G. Salmoria, A. Moré, J. Vassoler, E. Fancello, Torsion test method for mechanical characterization of PLDLA 70/30 ACL interference screws, Polym. Test. 34 (2014) 34–41.
[27] D. Farrar, Modelling of the degradation process for bioresorbable polymers, in: Degradation Rate of Bioresorbable Materials, Elsevier, 2008, pp. 183–206.
[28] J. Pan (Ed.), Modelling Degradation of Bioresorbable Polymeric Medical Devices, Woodhead Publishing, 2015.
[29] M. Ortiz, L. Stainier, The variational formulation of viscoplastic constitutive updates, Comput. Methods Appl. Mech. Engrg. 171 (3–4) (1999) 419–444.
[30] R. Radovitzky, M. Ortiz, Error estimation and adaptive meshing in strongly nonlinear dynamic problems, Comput. Methods Appl. Mech. Engrg. 172 (1–4) (1999) 203–240.
[31] T.E. Sayed, A. Mota, F. Fraternali, M. Ortiz, A variational constitutive model for soft biological tissues, J. Biomech. 41 (7) (2008) 1458–1466.
[32] J.M. Vassoler, L. Reips, E.A. Fancello, A variational framework for fiber-reinforced viscoelastic soft tissues, Internat. J. Numer. Methods Engrg. 89 (13) (2012) 1691–1706.
[33] J.M. Vassoler, L. Stainier, E.A. Fancello, A variational framework for fiber-reinforced viscoelastic soft tissues including damage, Internat. J. Numer. Methods Engrg. (2016) 865–884.

[34] N. Bleier, J. Mosler, A hybrid variationally consistent homogenization approach based on Ritz's method, Internat. J. Numer. Methods Engrg. 94 (7) (2013) 625–647.
[35] L. Brassart, L. Stainier, I. Doghri, L. Delannay, A variational formulation for the incremental homogenization of elasto-plastic composites, J. Mech. Phys. Solids 59 (12) (2011) 2455–2475.
[36] L. Brassart, L. Stainier, I. Doghri, L. Delannay, Homogenization of elasto-(visco)-plastic composites based on an incremental variational principle, Int. J. Plast. 36 (2012) 86–112.
[37] Q. Yang, L. Stainier, M. Ortiz, A variational formulation of the coupled thermo-mechanical boundary-value problem for general dissipative solids, J. Mech. Phys. Solids 54 (2) (2006) 401–424.
[38] L. Stainier, M. Ortiz, Study and validation of a variational theory of thermo-mechanical coupling in finite visco-plasticity, Int. J. Solids Struct. 47 (5) (2010) 705–715.
[39] L. Stainier, Consistent incremental approximation of dissipation pseudo-potentials in the variational formulation of thermo-mechanical constitutive updates, Mech. Res. Commun. 38 (4) (2011) 315–319.
[40] L. Stainier, Chapter two - A variational approach to modeling coupled thermo-mechanical nonlinear dissipative behaviors, in: S.P.A. Bordas (Ed.), Advances in Applied Mechanics, vol. 46, Elsevier, 2013, pp. 69–126.
[41] A. Bartels, T. Bartel, M. Canadija, J. Mosler, On the thermomechanical coupling in dissipative materials: A variational approach for generalized standard materials, J. Mech. Phys. Solids 82 (2015) 218–234.
[42] E. Fancello, J.-P. Ponthot, L. Stainier, A variational formulation of constitutive models and updates in non-linear finite viscoelasticity, Internat. J. Numer. Methods Engrg. 65 (11) (2006) 1831–1864.
[43] E. Fancello, J. Vassoler, L. Stainier, A variational constitutive update algorithm for a set of isotropic hyperelastic-viscoplastic material models, Comput. Methods Appl. Mech. Engrg. 197 (49–50) (2008) 4132–4148.
[44] J. Mosler, F. Cirak, A variational formulation for finite deformation wrinkling analysis of inelastic membranes, Comput. Methods Appl. Mech. Engrg. 198 (27–29) (2009) 2087–2098.
[45] J. Mosler, On variational updates for non-associative kinematic hardening of Armstrong-Frederick-type, Tech. Mech. 30 (1–3) (2010) 244–251.
[46] L. Brassart, L. Stainier, On convergence properties of variational constitutive updates for elasto-visco-plasticity, GAMM-Mitt. 35 (1) (2012) 26–42.
[47] O. Kintzel, J. Mosler, A coupled isotropic elasto-plastic damage model based on incremental minimization principles, Tech. Mech. 30 (1–3) (2010) 177–184.
[48] O. Kintzel, S. Khan, J. Mosler, A novel isotropic quasi-brittle damage model applied to {LCF} analyses of Al2024, Int. J. Fatigue 32 (12) (2010) 1948–1959.
[49] O. Kintzel, J. Mosler, An incremental minimization principle suitable for the analysis of low cycle fatigue in metals: A coupled ductile-brittle damage model, Comput. Methods Appl. Mech. Engrg. 200 (45–46) (2011) 3127–3138.
[50] A. Siddiq, R. Arciniega, T. El Sayed, A variational void coalescence model for ductile metals, Comput. Mech. 49 (2) (2012) 185–195.
[51] M. Canadija, J. Mosler, A variational formulation for thermomechanically coupled low cycle fatigue at finite strains, Int. J. Solids Struct. 100–101 (2016) 388–398.
[52] J. Mosler, M. Ortiz, Variational h-adaption in finite deformation elasticity and plasticity, Internat. J. Numer. Methods Engrg. 72 (5) (2007) 505–523.
[53] J. Mosler, O. Bruhns, Towards variational constitutive updates for non-associative plasticity models at finite strain: Models based on a volumetric-deviatoric split, Int. J. Solids Struct. 46 (7–8) (2009) 1676–1684.
[54] A. Needleman, Material rate dependence and mesh sensitivity in localization problems, Comput. Methods Appl. Mech. Engrg. 67 (1) (1988) 69–85.
[55] S. Murakami, M. Kawai, H. Rong, Finite element analysis of creep crack growth by a local approach, Int. J. Mech. Sci. 30 (7) (1988) 491–502.
[56] S. Murakami, Y. Liu, Mesh-Dependence in local approach to creep fracture, Int. J. Damage Mech. 4 (3) (1995) 230–250.
[57] R. Peerlings, M. Geers, R. de Borst, W. Brekelmans, A critical comparison of nonlocal and gradient-enhanced softening continua, Int. J. Solids Struct. 38 (44–45) (2001) 7723–7746.
[58] N. Moës, C. Stolz, P.-E. Bernard, N. Chevaugeon, A level set based model for damage growth: The thick level set approach, Internat. J. Numer. Methods Engrg. 86 (3) (2010) 358–380.
[59] P. Bernard, N. Moës, N. Chevaugeon, Damage growth modeling using the Thick Level Set (TLS) approach: Efficient discretization for quasi-static loadings, Comput. Methods Appl. Mech. Engrg. 233–236 (2012) 11–27.
[60] C. Stolz, N. Moës, A new model of damage: a moving thick layer approach, Int. J. Fract. 174 (1) (2012) 49–60.
[61] J. Chaboche, A review of some plasticity and viscoplasticity constitutive theories, Int. J. Plast. 24 (10) (2008) 1642–1693. Special Issue in Honor of Jean-Louis Chaboche.
[62] G. Weber, L. Anand, Finite deformation constitutive equations and a time integration procedure for isotropic, hyperelastic-viscoplastic solids, Comput. Methods Appl. Mech. Engrg. 79 (2) (1990) 173–202.
[63] J.S. Soares, Constitutive Modeling of Biodegradable Polymers for Application in Endovascular Stents (Ph.D. thesis), Texas A&M University, 2008.
[64] E.A. de Souza Neto, D. Peric, D.R. Owen, Computational Methods for Plasticity: Theory and Applications, John Wiley & Sons, Ltd., 2008.
[65] H. Li, M. Fu, J. Lu, H. Yang, Ductile fracture: Experiments and computations, Int. J. Plast. 27 (2) (2011) 147–180.
[66] C.K. Bynum, Failure mode of suture anchors as a function of insertion depth, Amer. J. Sports Med. 33 (7) (2005) 1030–1034.
[67] C.M. Hughes, A. Bordush, B. Robioneck, P. Procter, C.J. Brown, Bone anchors - A preliminary finite element study of some factors affecting pullout, J. Med. Devices 8 (4) (2014) 041006.1–041006.9.
[68] A.E. Selke, Variational Models of Thermo-Viscoelastic Damage: Applications to Polymer Behavior and Coupling with Thick Level Set Approach to Nonlocal Dama (Ph.D. thesis), Ecole Centrale de Nantes, France, Universidade Federal de Santa Catarina, Brazil, 2016.